UNIVERSITÀ DEGLI STUDI DI PADOVA

Dipartimento di Fisica e Astronomia “Galileo Galilei”

Corso di Laurea Triennale in Fisica

Tesi di Laurea

Sviluppo di un Calorimetro Acromatico per Protoni in ambito medico

Relatore
Prof. Piero Giubilato

Laureanda
Chiara Bonini

Anno Accademico 2017/2018

Summary

1 Introduction

iMPACT, *innovative Medical Proton Achromatic Calorimeter and Tracker*, is a University of Padua and INFN project, funded by the *European Research Council*. The project aim is to design, develop and prototype an extremely fast and accurate *proton Computed Tomography Scanner*, with the ultimate goal of enabling the realization of a clinically viable proton Computed Tomography (pCT) system. Proton Computed Tomography is an extremely promising technique able to reconstruct density maps of the human body with minimal dose release and high accuracy on tissue density, a particularly critical feature in cancer Hadron-Therapy treatment planning. Hadron-Therapy is a leading edge technique where protons or heavy-ions, instead of X-rays, are used to target and destroy a tumor within the human body. By exploiting the peculiar energy deposition distribution of hadrons, it is in fact possible to confine within a volume of few mm^3 most of the energy released, hence sparing the healthy tissues surrounding the tumor.

However, despite all its beneficial aspects, Hadron-Therapy is not yet widespread as other more established procedures, such as X-ray therapy. In particular, imaging techniques based on X-ray Computed Tomography (X-ray CT), currently used to produce body density maps, cannot provide information accurate enough to exploit the intrinsic accuracy of the hadron treatment. It is in fact necessary to possess very accurate knowledge of the density of the tissues crossed by the proton before reaching the tumor in order to precisely aim its energy release with millimeter precision. The idea standing behind the development of a pCT scanner is that using the same energy loss behavior for both the imaging process and the treatment would improve the performance of the latter, the physical interaction being the same. Currently, several pCT scanner prototypes are being developed around the world; pCT scanner technology however is still far from being applicable in a clinical environment, mainly due to the slow acquisition rates. The iMPACT project therefore plans to develop a pCT scanner able to overcome such limitation, leading the way towards sound and medical-grade apparatuses.

This thesis begins by displaying both limitations and advantages of the Hadron Therapy technique; the pCT state-of-the-art is then reviewed, highlighting positive features as well as constraints that limit its applicability. The current state of development of the the iMPACT scanner, which embeds a tracker system and a calorimeter, is illustrated and

discussed, focusing on the study of data collected with proton beams for the qualification of the iMPACT calorimeter and the development of future prototypes.

2 Proton-Therapy

In present days, tumors are the main cause of death in developed countries and the second one in developing countries (1). Currently the most used medical procedures to cure these tumors consist in surgery, chemotherapy and X-ray therapy, with the latter used in more than 40% of the patients affected by localized malignant tumors (2).

2.1 Comparison between X-rays, protons and heavy ions in cancer treatment

X-ray therapy relies on using MeV-scale photons to deliver ionizing radiation dose in organic tissues; the deposited energy can damage the molecules inside cells, including the DNA, therefore hindering cellular reproduction. The photon dose-depth profile reaches its maximum a few cm under the surface, decreasing exponentially afterwards, due to photons absorption in the material, as shown in Figure 2.1.

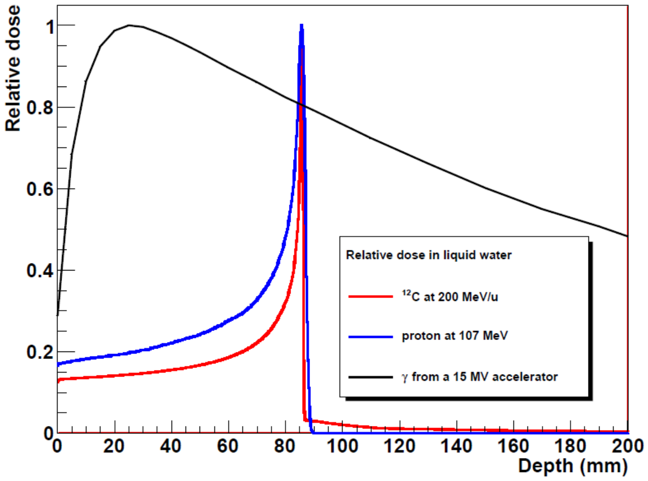

Figure 2.1: Dose-depth profile in water for X-rays, protons and carbon ions (23).

This behavior impairs the capability to accurately target a limited volume without significantly affecting surroundings tissues. To limit this issue X-ray treatments often target the tumor from multiple directions, to spread the non-necessary dose over a larger volume, as shown in Figure 2.2.

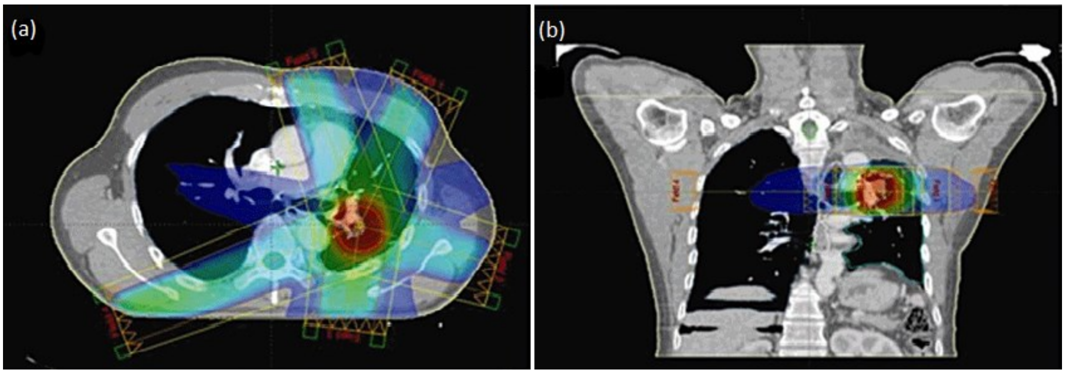

Figure 2.2: Example of treatment plan for lung cancer, with dose distribution. Axial view of an intensity-modulated X-ray radiotherapy plan (a) and the coronal view (b). (24)

Unlike photons, massive-charged particles release their energy proportionally to the inverse of the square of their velocity, according to the Bethe-Bloch formula (3) (4):

$$-\left\langle\frac{dE}{dx}\right\rangle = \frac{4\pi}{m_e c^2}\,\frac{nz^2}{\beta^2}\left(\frac{e^2}{4\pi\varepsilon_0}\right)^2\left[ln\left(\frac{2m_e c^2\beta^2}{I\,(1-\beta^2)}\right)-\,\beta^2-\frac{\delta}{2}-\frac{C}{Z}\right] \qquad [\,1\,]$$

Where m_e is the electron mass, β is the projectile speed in units of c, z is the projectile electric charge, I is the mean excitation potential of the material, δ is the outer electrons shielding correction, C is a shell-correction parameter and the electron density per unit volume n can be calculated with:

$$n = \frac{N_A Z\rho}{AM_u} \qquad [\,2\,]$$

where N_A is the Avogadro number, Z and A are the material atomic and mass number respectively, ρ is the mass density of the absorbing material and $M_u = 1$ g/mol.

The dose-depth profiles of massive-charged particles present a maximum, the *Bragg peak*, located close to the end of the particle path, while the energy deposition before the peak is rather low (about 20% of the maximum) and almost absent after the peak, as shown in Figure 2.1.

Cancer treatment with X-rays targets the tumor from different angles to optimize the dose distribution and minimize the damage to the neighborhood tissues. In hadron therapy instead, the hadron energy is tuned to achieve the same effect (tumor painting) with a much higher precision. In fact, a number of hadron beams are calibrated so that the total deposited dose presents a constant profile, called Spread Out Bragg Peak (SOBP), at the depth corresponding to the tumor volume (Figure 2.3). This method implies a higher dose released before the SOBP than the use of a single particle, depending on the number of beams used to paint the area, yet lower than in X-ray.

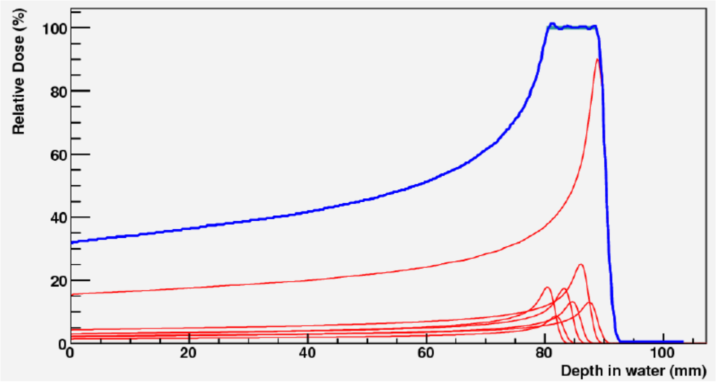

Figure 2.3: A Spread Out Bragg Peak (blue) created from the sum of several protons beams with different energies and flux (red).

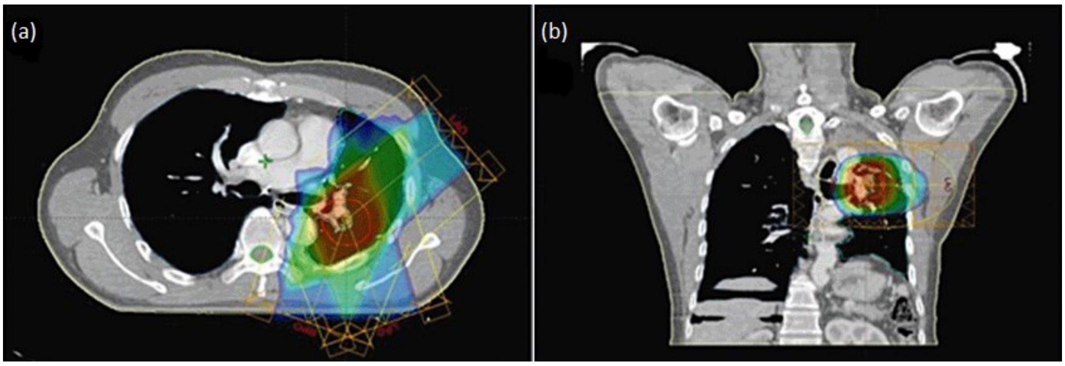

Figure 2.4: Example of treatment plan for lung cancer, with dose distribution. Axial view of a proton beam therapy (PBT) plan (a) and the coronal view (b). (24)

Beyond the dose depth-profile characterized by the Bragg peak, another advantageous feature of protons and ions over photons is their biological effectiveness, described by the relative biological efficiency factor (RBE). The RBE is defined as the ratio between the doses deposited by photons D_{phot} in respect with dose deposited by a given hadron D_{hadr} in order to cause the same damage to the biological tissue

$$RBE = \frac{D_{phot}}{D_{hadr}}. \qquad [3]$$

The biological damage can be quantified by the fraction of cells S surviving after the deposition of a dose D. Data of the survival fraction S can be parametrized by a linear-quadratic model, with α e β experimentally determined parameters (5):

$$S(D) = e^{(-\alpha D - \beta D^2)}. \qquad [4]$$

From the definition of RBE and from Figure 2.5, it can be appreciated how the same survival fraction S is obtained with a lower dose deposited by heavy ions respect to the dose deposited by X-rays. This behavior makes them better candidates for cancer treatment than photons.

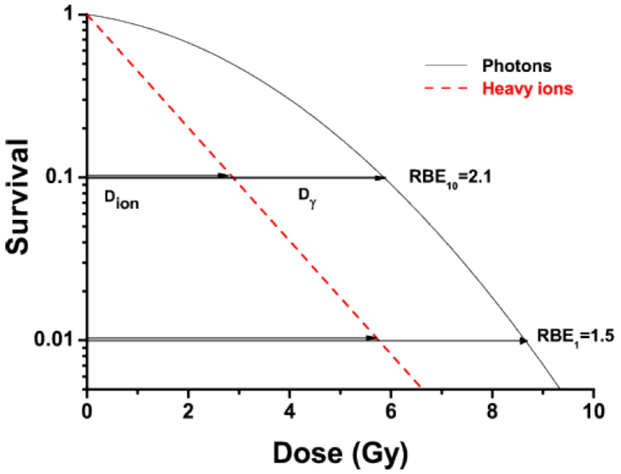

Figure 2.5: Survival fraction as a function of dose for photons and a generic heavy ion.

Ions with higher masses have usually higher RBE values, for example carbon reaches a RBE of ≈ 3, and therefore are more effective than lighter ions, such as protons.

2.2 Proton Range

Protons travel through matter, continuously losing energy by Coulomb interactions with atomic electrons, which to a first order do not have enough mass to affect the proton direction. Protons also interact via Coulomb elastic scattering with the positive-charged atomic nuclei, which can deflect the particle trajectory, being the differential cross section described by Rutherford's relation (6):

$$\frac{d\sigma}{d\Omega} = z^2 Z^2 r_e^2 \left(\frac{m_e c}{4\beta p}\right)^2 sen^{-4}\left(\frac{\theta}{2}\right) \qquad [5]$$

where θ is the scattering angle, Ω is the solid angle, r_e is the classical electron radius and p is the particle momentum. From the above formula is apparent how small deflections are favored.

Nuclear scattering is also possible but less frequent (around 15% of 200 MeV protons undergo nuclear inelastic reactions along their path); in this case a proton overcomes the Coulomb nuclear barrier, interacting inelastically with the atomic nucleus. The reaction can produce neutrons, secondary protons, γ-rays or light ions. The secondary protons produced via nuclear interactions are responsible of about 10% of the total dose deposited by a 200 MeV proton beam (7).

The Bethe-Bloch formula describes the mean energy loss rate per unit length, called *Stopping Power*, which is released from the Coulomb interactions of projectile particles with electrons of the material. The *Stopping Power* is strictly related to the absorbing material properties, most strongly to the material density, whose values can cover a range of three orders of magnitude in a human body, from air in the lung (0.0012 g/cm^3) to cortical bone (up to 2 g/cm^3). It is clear that precisely knowing the tissues density distribution is essential to plan a proton therapy treatment with sufficient accuracy (7).

The range of a particle beam, considering the particles path linear and neglecting the lateral scattering can be defined from the stopping power and the particle energy E as:

$$R(E) = \int_0^E \left\langle \frac{dE'}{dx} \right\rangle^{-1} dE' \,. \qquad [\,6\,]$$

A relation between the particle energy and its range was found by Bragg and Kleeman in 1905 and it is expressed from an analytical expression where α and p are absorber and particle dependent parameters derived experimentally (8) (9) (10):

$$R(E) = \alpha E^p \,. \qquad [\,7\,]$$

Proton range of interest in hadron therapy typically goes up to about 30 cm (the deepest site in the human body), while the required accuracy for the proton stopping position is about 1 mm (the typical voxel size in medical imaging) (7).

However, the real particle path is not straight because of the single inelastic Coulomb scattering, which integrated over a wide number of collisions leads to statistical fluctuations of the energy loss rate. The dispersion causes a spread of the particle range around its mean value, called Range Straggling. The energy lost by a particle beam passing through a thin layer of material is therefore distributed accordingly to an asymmetric Landau distribution(11) (12). However, in the limit of many collisions (thick layers) a Gaussian distribution can approximate this asymmetric energy loss distribution. Experimental values of range and range straggling for protons with varying energies in different materials have been measured and tabulated (13); for ~ 200 MeV protons, the range straggling stands between 0.9% and 1.2% of the total range. The range straggling establishes an intrinsic limit to the precision with which particle ranges can be predicted and measured.

In proton Tomography, the range path length is usually described by WEPL (Water Equivalent Path Length), which consists in the integral along the proton path L inside the absorber material of the relative stopping power RSP, defined as ratio between the stopping power of the material and the stopping power of water:

$$RSP = \frac{S_{material}}{S_{water}} \qquad [\,8\,]$$

$$WEPL = \int_0^L RSP(l)dl \qquad [\,9\,]$$

where $RSP(l)$ is the relative stopping power at l distance along the path.

2.3 Limits of Proton-Therapy and pCT Scanner

The effectiveness of the hadron-therapy technique is strongly related to the accuracy of the knowledge of the patient tissues density map, which is necessary to precisely calibrate the proton beam energy, in order to match the Bragg peak with the tumour volume.

Currently, 3D maps of the patient tissues can only be obtained with X-ray Computed Tomography (X-ray CT). This technique can not produce density maps accurate enough to fully exploit the intrinsic accuracy of the Hadron-Therapy procedure, mainly because of the different behaviour inside matter between hadrons and photons (14).

A proton Computed Tomography (pCT), would improve both the accuracy of the imaging process and the effectiveness of the treatment, as the particles used for both present the same energy-loss behaviour (15). Proton Tomography techniques have not become clinically viable technologies yet, as opposed to the widely established X-ray CT technique, due to physical, experimental and accessibility limitations. A relevant physical limitation is given by the multiple Coulomb scattering of the proton in matter, which is the main reason for the worse spatial resolution of pCT. The other major limitation is given by the slow experimental acquisition rate of the current pCT prototypes. With the best present setup, which reaches a 2 MHz acquisition rate, a complete record of the 10^9 required proton tracks-energy information would take about 10 minutes to be completed. With such long scanning time, the image quality becomes affected by motion of internal organs, mainly due to the patient's breathing. Shorter scanning time, in the order of 10 seconds or less, would allow patients to hold their breath for the duration of the procedure, a measure already applied in hold-breath X-ray CT (16).

Hadron-therapy diffusion is still limited, mostly due to the high costs of the construction and operation of these facilities, including accelerators, beam lines, and patient delivery systems (gantries) and their maintenance. The number of patients treated with protons or heavier ions is still a small fraction of the total number of tumor-affected patients, with the X-ray therapy being the most common procedure, despite the fast growth of the number of protons and ions therapy centers. The cost of a proton treatment, in fact, was calculated to be roughly twice than the cost of a photon treatment (17). Nevertheless, an effective pCT system would boost the hadron-therapy treatment effectiveness, further increasing its value as therapeutic solution, and therefore its diffusion.

3 The iMPACT Project

iMPACT is a European Research Council Consolidator Grant funded project (18), hosted by University of Padua and supported by INFN. The iMPACT project is born to develop a high resolution and extremely fast proton Computed Tomography scanner for cancer treatment.

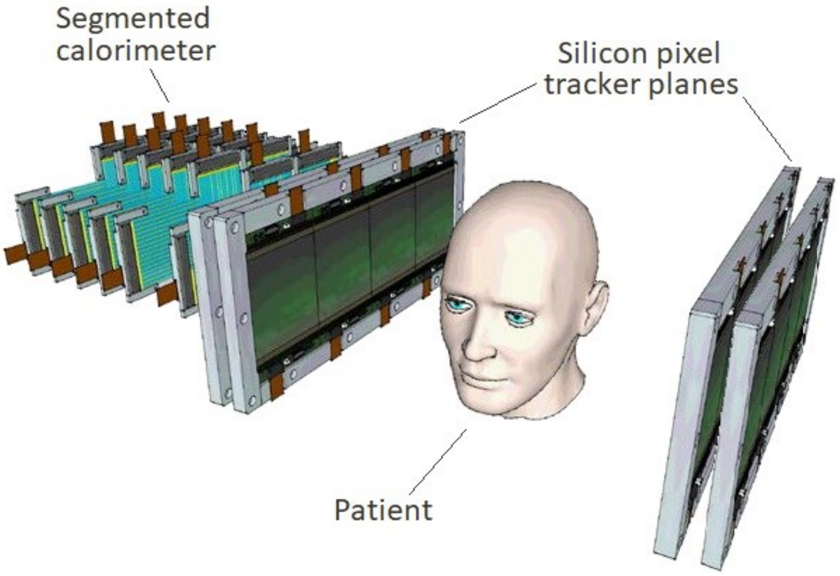

Figure 3.1: Rendering of the iMPACT scanner design

The iMPACT scanner consists of four silicon pixel sensors tracking planes and a highly segmented plastic scintillator calorimeter, as shown in Figure 3.1. The tracking planes are grouped in two stations of two layers each to allow for the measurement of the protons trajectory before and after passing through the patient's body.

3.1 Overview of the tracking system

The tracking system consists of four layer of silicon Monolithic Active Pixel Sensors. For the prototyping phase, the iMPACT scanner adopts the ALPIDE sensor. The ALPIDE sensor has been developed within the ALICE collaboration for the upgrade of its Inner Tracking System. This sensor is a 100µm thick, 1.5cm x 3cm large silicon Monolithic Active Pixel Sensor (MAPS) featuring 28µm x 28µm pixels arranged in a 512 x 1024 matrix. Each pixel output is binary, being it 1 when the ionization due to a charged particle hitting the detector is higher than a given threshold. The sensor is able to cope with a 100 kHz/cm2 particle rate, most limited by the read-out bandwidth of 1.2 Gbit/s. The charge collection in the ALPIDE sensor can be enhanced by applying a reverse bias to the substrate, which for proton detection helps in controlling the spread of the charge itself, limiting the number of pixels firing for a given hit.

3.2 The Calorimeter

The iMPACT calorimeter operates as a range calorimeter, estimating the proton stopping position instead of directly measuring the residual proton energy. The complete calorimeter consists of about 60 planes of 5mm thick plastic scintillators, covering surface area of about 20 x 20 cm^2. Every plane of plastic scintillator is also divided into smaller segments, called *fingers*, each 1cm wide and 20cm long. *Fingers* of consecutive planes are mutually orthogonal.

This calorimeter segmentation allows to read each *finger* with a single Silicon Photo Multiplier (SiPM). Each *finger* is wrapped with a thin, highly reflective Teflon layer, to improve light collection. When the proton stops, the range, in a first approximation, is assumed to be equal to the length between the first hit layer and the mean point of the last layer hit, with an uncertainty given by the thickness of the sensitive element (5mm) divided by $\sqrt{12}$. The estimation of the proton stopping position can be refined using the information on the energy deposited in each finger along the proton path. The SiPM signals amplitudes outline the Bragg curve profile, which can be fitted in order to calculate the proton stopping position with a resolution up to 1mm (19).

The fingers are made of Polyvinyl Toluene (PVT) BC-408 scintillators, featuring a fast time response (a few ns) high light yield (11136 photons/MeV), and a peak light emission wavelength around 425nm.

The Silicon Photon Multiplier (SiPM) is a solid-state photon-counting device and it is developed for low light level detection. The active area of the SiPM is smaller than a cm^2 and the efficiency of this device is up to 40% with a low operating voltage of ~60V. It has a good time resolution, up to 250ps, and it is unaffected by magnetic fields. The SiPM sensitive surface consists in a matrix of multiple APD (Avalanche Photodiode) pixels operating in Geiger mode so that the electron gain is 10^5-10^6 and the output current of each APD is constant and independent from the number of incident photons. The time necessary for the APD to switch off the Geiger avalanche and being able to detect a new photons after a photon hit is called *quenching time* t_{quench}, which spans a range between 20ns and 150ns in different SiPM devices. The SiPM output signal consists in the sum of single current signals from each hit pixel, each with the same amplitude, so that the total signal is proportional to the number of pixels hit. The relation is linear as long as the number of simultaneous photons is low enough to have a negligible probability for two or more photons to hit the same APD.

The SiPM chosen for the iMPACT project are Hamamatsu S12572-025c 3mm x 3mm SiPM with 25µm pixel pitch and a detection efficiency that peaks around a 450nm wavelength, matching the PVT emission. The quenching time for this SiPM model was roughly estimated to be around 100 ns.

The calorimeter is made by identical, modular blocks, each consisting of 32 fingers arranged in four parallel planes, as shown in Figure 3.2. A single unit holds the scintillating fingers, the SiPM read-out electronics and the input-output ports. A sector of the calorimeter is assembled by combining two orthogonally rotated modules. Finally, a complete layer consists of four sectors tiled together.

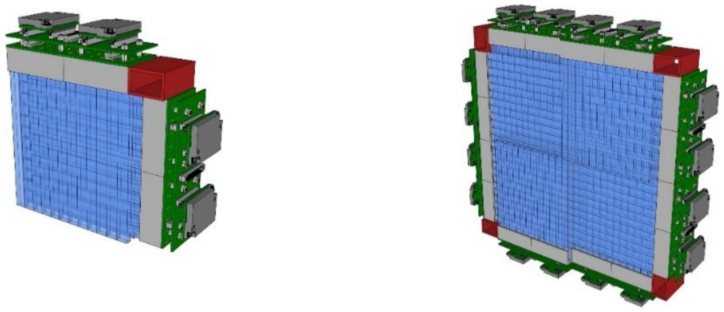

Figure 3.2: A combination of two iMPACT calorimeter modular units forming an angular sector (left) and a complete layer (right).

The complete calorimeter consists in 60 planes of 32 fingers each, so the number of SiPM output channels would be extremely high, and the analog recording of every single waveform would be impractical. The chosen approach consists in continuously sampling each SiPM analog output at high frequency (> 200MHz) into a 3 or 4 levels digital value, in order to minimize the amount of data to be driven off-detector. Only digital outputs are further processed.

4 Simulations and tests of the calorimeter readout

4.1 Measurement of the SiPM response to a single photon

The calorimeter read-out chain characterization started with an evaluation of the signal produced by the detection of a single photon on the SiPM. In this way, the electronics parameters (such as gain and dynamic range) could therefore be adjusted accordingly to the expected number of detected photons.

The study of a single photon signal is based on the measurement of the signals produced by a countable and low number of simultaneous photons hitting the SiPM. The equipment used for the measurement consists of a PicoQuant PLS-592 pulsed LED, which is detected with the full SiPM read-out chain, and a Teflon surface. The entire apparatus is enclosed in a sealed dark chamber, to isolate the instruments from external light sources. The analog SiPM output waveform is captured, digitized and saved into a file by a Tektronix DPO 7354 fast oscilloscope, with the external trigger driven by the pulse generator. A delayed coincidence with the driver pulses “around 2ns” is used to reject dark-count signals and room background.

The emitting diode is driven such that to minimize the emission intensity and the number of photons detected by the SiPM is therefore less than 10. Each digitized waveform is fit with a Gaussian function with a fixed width interval around the maximum.

The spectrum of waveform amplitudes, obtained with the Gaussian fit, Figure 4.1, presents equally spaced peaks, each one associated to events with a discrete consecutive number of simultaneous photons. Features of a Poisson distribution can be clearly seen.

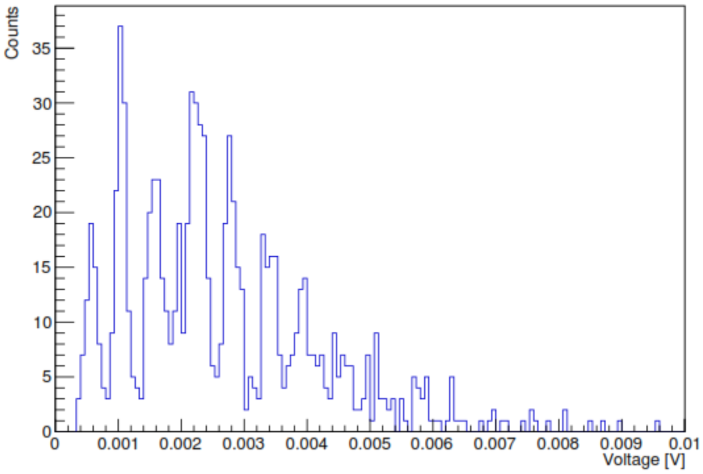

Figure 4.1: Spectrum of few-photons waveform amplitudes obtained with the Gaussian fit.

To estimate the amplitude of a single photon signal, the ratio between the peak centroids and the associated number of photons of the first eight peaks was calculated.

The dependence of the centroids of the peaks of the spectrum, from the number of photons, is approximately linear, with a 0.578 mV / photons proportionality coefficient and a -0.08 mV intercept (Figure 4.2).

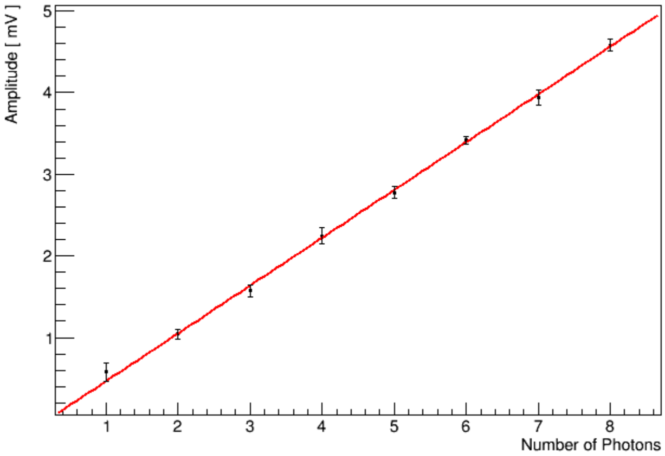

Figure 4.2: Signal amplitude as a function of number of photons and linear fit.

The linearity confirms the correct association of each peak with the respective photon count, so it is possible to consider each waveform and to compare the single photon waveform obtained from the different families of photons signals, normalized by the respective number of photons. The baseline is calculated as the average amplitude in the first 10 ns, and is subtracted from each waveform. Figure 4.3 shows the overlap of the mean single photon waveform calculated from different families of photon signals. The events relative to a single detected photon are discarded, due to being highly affected by background noise.

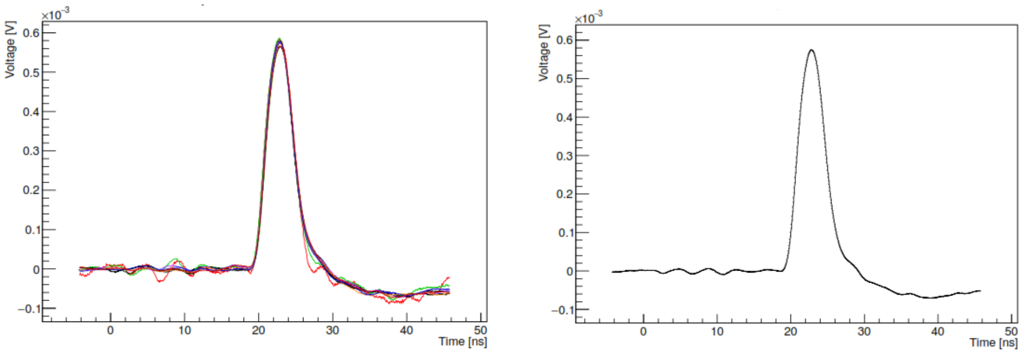

Figure 4.3: Overlap of average single photon waveforms obtained separately from families of photons from 2 to 9 (left); average single photon waveform (right).

Figure 4.3 (right) shows the average single photon signal, obtained from the events with 3 or more photons. The averaged single photon signal presents a maximum of 0.575 mV, a raise time of about 3 ns, a decay time of about 5 ns and then flattens to a negative value of amplitude (undershoot) caused by the SiPM read-out electronics.

4.2 Evaluation of the linearity of the SiPM response

A Monte Carlo simulation of the calorimeter has been developed in order to evaluate its performance. The simulation has been used, in a first phase, to optimize the detector constructive parameters, while, in a more advanced stage, it will provide experimental-like output data for testing the read-out chain, the data analysis software, and the image reconstruction techniques.

The simulation was modelled using the GATE application, an advanced open source software dedicated to numerical simulations in medical imaging and radiotherapy (20), based on the Geant4 toolkit (21). The interface provided by GATE to the Geant4 libraries allows to define volumes, materials and their physical properties to each volume, including density, atomic number and optical properties. Different kind of particle sources can be defined, from pencil-beams to emitting volumes, with customizable energy spectra and particle rate. Moreover, particle detectors can be implemented, with parameterized response and read-out chain.

Each single APD cell that composes the SiPM sensitive surface features a dead time, or quenching time tquench, therefore additional photons reaching the same APD cell within tquench after the detection of a photon, are lost. This feature is a source of non-linearity between the number of photons reaching the SiPM surface and the output signal ampitude, particularly present in case of high photon fluxes. To estimate this non-linearity, a series of simulations are performed in order to quantify the fraction of photons lost due to the quenching time.

The simulation uses a mono-energetic 230 MeV proton pencil beam, two PVT fingers and a Plexiglas volume between the fingers to simulate an absorber. Protons pass through the first finger with their full energy, so that the energy deposition inside this finger is at its minimum, corresponding to the initial part of the Bragg Curve. The absorber volume thickness was set to be about 28 cm, in order to have the protons stopping inside the second finger. With this configuration, the proton beam deposits all the residual energy in the second finger, where the Bragg Curve presents the proton Bragg peak. The time duration of the simulated beam is set to 100 ns, the measured quenching time.

GATE provides the impact position of each detected photon on the SiPM sensitive surface; therefore, it is possible to observe if an APD cell is hit more than once. The number of detected photons, in the realistic case of tquench = 100 ns, is given by the total number of hit cells. The number of detected photons in the ideal case of tquench = 0 ns is instead given by the total number of hits; both are presented in Figure 4.4 for the initial part of the curve and in the proximity of the Bragg peak. Errors associated at each point are calculated as the standard deviation over several repeated simulations.

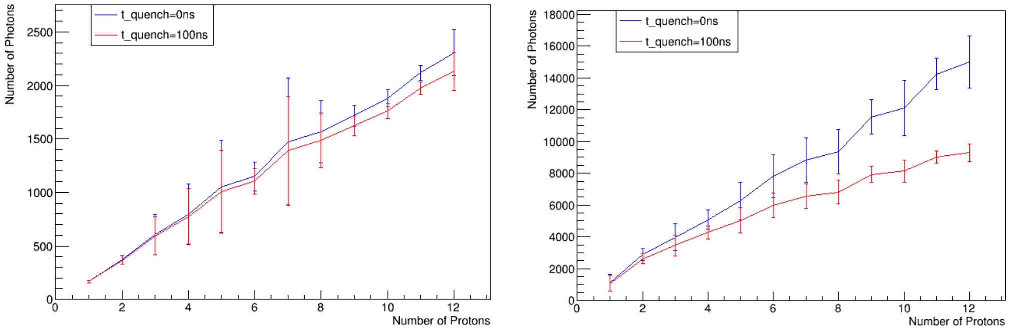

Figure 4.4: Number of detected photons as a function of the proton flux on a single PVT finger in the ideal case with t_{quench}*=0 ns (blue) and in the realistic case with* t_{quench}*=100 ns (red). Energy released corresponding to the initial region of the Bragg Curve (left) and to the Bragg peak (right).*

The fraction of lost photons in the plateau is almost negligible, within the error bars, while in correspondence of the Bragg peak the fraction of lost photons reaches almost the 40% with 12 protons/100 ns, corresponding to a 120 MHz acquisition rate. In the latter condition the non-linearity between the numbers of photons reaching the SiPM and the number of detected photons is clearly visible.

The finger efficiency accounting for the quenching time effect can be calculated as the ratio between the number of detected photons in the realistic case tquench = 100 ns and the ideal case tquench = 0 ns, and has to be multiplied for the intrinsic SiPM efficiency, in order to obtain the total detection efficiency. The effect of tquench on the efficiency is shown in Figure 4.5. In the first finger the efficiency remains higher than 90% with more than 10 protons per 100 ns, which corresponds to a 100 MHz rate, while the finger placed on the Bragg peak, maintains an efficiency higher than 90% with less than 3 protons per 100 ns, equal to 30 MHz.

However, the duration of the analog signal is about 50 ns, therefore the proton rate in a single finger cannot be higher than 10 MHz, in order to avoid signal pile-up (equivalent to 1proton/100ns on average).

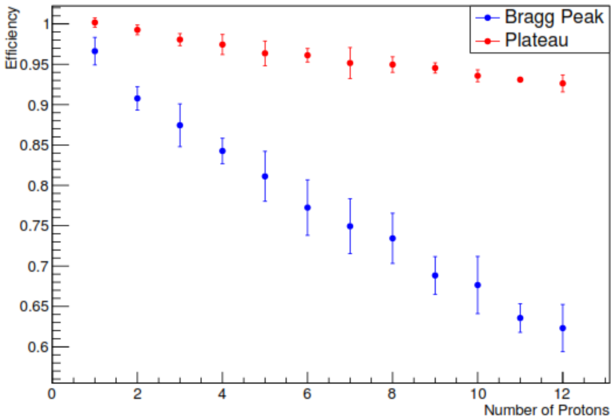

Figure 4.5: Detection inefficiency due to quenching time as a function of the number of protons in 100 ns.

5 Characterization of calorimeter elements with proton beam data

After the characterization of the single calorimeter components, a test was conducted in July 2017 at the experimental line of the *Trento Institute for Fundamental and Applied Physics* (TIFPA) hosted at *Azienda Provinciale per I Servizi Sanitari* (APSS) proton therapy facility in Trento. The APSS facility is built around an IBA Proteus 235 cyclotron, which can accelerate protons at energies between 70 MeV and 228 MeV, and includes two medical treatment rooms and a dedicated line for science and research, administered by TIFPA. The beam energy can be lowered down to 15 MeV, in the experimental line, by using appropriate degraders, while the beam size is about 1 cm FWHM.

5.1 Description of the experimental setup

The apparatus mimics a small portion of the range calorimeter by aligning to the beam axis two rows of 4 scintillator fingers each, as shown in Figure 5.1. The topmost row is composed of BC-408 scintillators while the other row is composed of BC-420 scintillators.

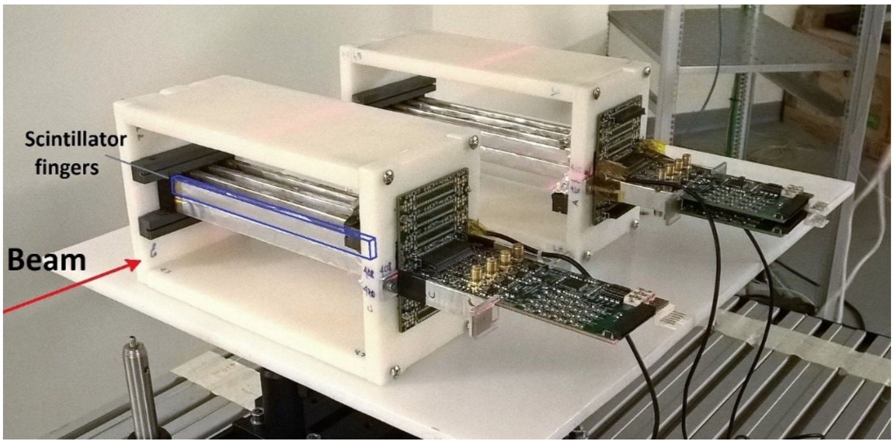

Figure 5.1: Setup used for the test at the TIFPA experimental beam line in Trento.

Each scintillator is wrapped with a Teflon layer, to enhance light collection efficiency and a protective aluminum foil, for a total aluminum thickness of about 800µm. Every scintillator is connected to a SiPM, the BC-408 scintillators and two BC-420 scintillators are connected to the Hamamatsu S12572-025c SiPM, while the other BC-420 scintillators are connected to another type of SiPM, 1mm x 1mm Hamamatsu S12571-015C, faster but smaller, for comparison.

Two PSI DRS4 DAQ boards (22) read the SiPM and digitize the analog signals. In front of the two modules, an ALPIDE sensor was positioned for an independent characterization.

The setup included various movable Plexiglas absorbers with different thickness. The total thickness of the absorber plus the 8 PVT fingers was chosen to be equivalent to about 28 cm of Plexiglas, in order to stop 228 MeV protons, based on the simulation results. The relative positions of the calorimeter modules and the absorber could be modified in order to measure the proton energy release in different configurations. The read-out electronic generates a trigger when there is a coincident signal in two or more different fingers, selectable at will. The different configurations used in the test are summarized in Table 5.1.

	Configuration	**Energy [MeV]**
Run 4	4 BC-408 + 272 mm absorber + 4 BC-408	228
Run 5	282 mm absorber + 8 BC-408	228
Run 7	292 mm absorber + 8 BC-408	228
Run 8	8 BC-408	228
Run 10	2 BC-420 not read + 2 BC-420 read + 4 BC-408	70
Run 12	8 BC-408	35

Table 5.1: Considered configurations for the test at the TIFPA experimental beam line in Trento.

While simulations proved crucial in correctly dimensioning the various components during the design phase, the test beam did actually allow to fine-tune each of them. The acquisition rate for all the configurations was set to 2kHz. In configurations featuring BC-420 scintillators, only the signals coming from the two BC-420 scintillators connected to the 3mm x 3mm Hamamatsu SiPM, in addition to the usual BC-408 scintillators, are read-out, even if the proton beam passes through all the scintillators. Furthermore, the rows of BC-420 and BC-408 scintillators are at different heights, so that events from different scintillators rows in the same configuration are uncorrelated.

For each configuration, data are collected at various SiPM bias voltages in order to identify the best operating conditions for the apparatus.

5.2 Analysis of collected data with different configurations

The deposition energy of a proton beam is proportional to the signal pulse amplitude, so we did look at the signal amplitude as a function of the thickness of the material crossed. When all the events collected during the test are considered, the curve obtained with the averages of the signals pulse amplitudes does not show the expected clear shape of the energy deposition profile. This can happen because a significant fraction of the detected protons does not release their entire residual energy inside the fingers. In fact, fingers cover only 1cm in the vertical direction, so protons passing through the first one could deviate from a linear trajectory enough to miss the next. To avoid this problem, various trigger configuration have been tested. The triggers are bound with an AND operation, so that only when all the triggered channels see a proton passing through them, the event is collected by the read-out electronics.

For each SiPM recorded analog signal, the baseline is calculated as the average of the first 20ns, and then is subtracted from the signal amplitude, before calculating the maximum value. While the SiPM demonstrated a remarkable gain uniformity, nevertheless a scaling factor to normalize their gain has been introduced in the analysis. The scaling factors to normalize the SiPM gains have been obtained with the study of the configuration of Run 8. This configuration does not present the absorber, so it is useful for studying the initial part of the energy deposition profile for a proton beam at 228 MeV. The configuration presents two trigger channels, the 1st and the 5th. Figure 5.2 shows the maxima amplitudes distributions of signals for the eight channels. The signal distributions in the channels for this configuration show a lower mean for the 4th channel and introduce a problem for the 5th channel, because it presents an average higher than the other channels, and this is linked to the strange distribution of the events in this channel.

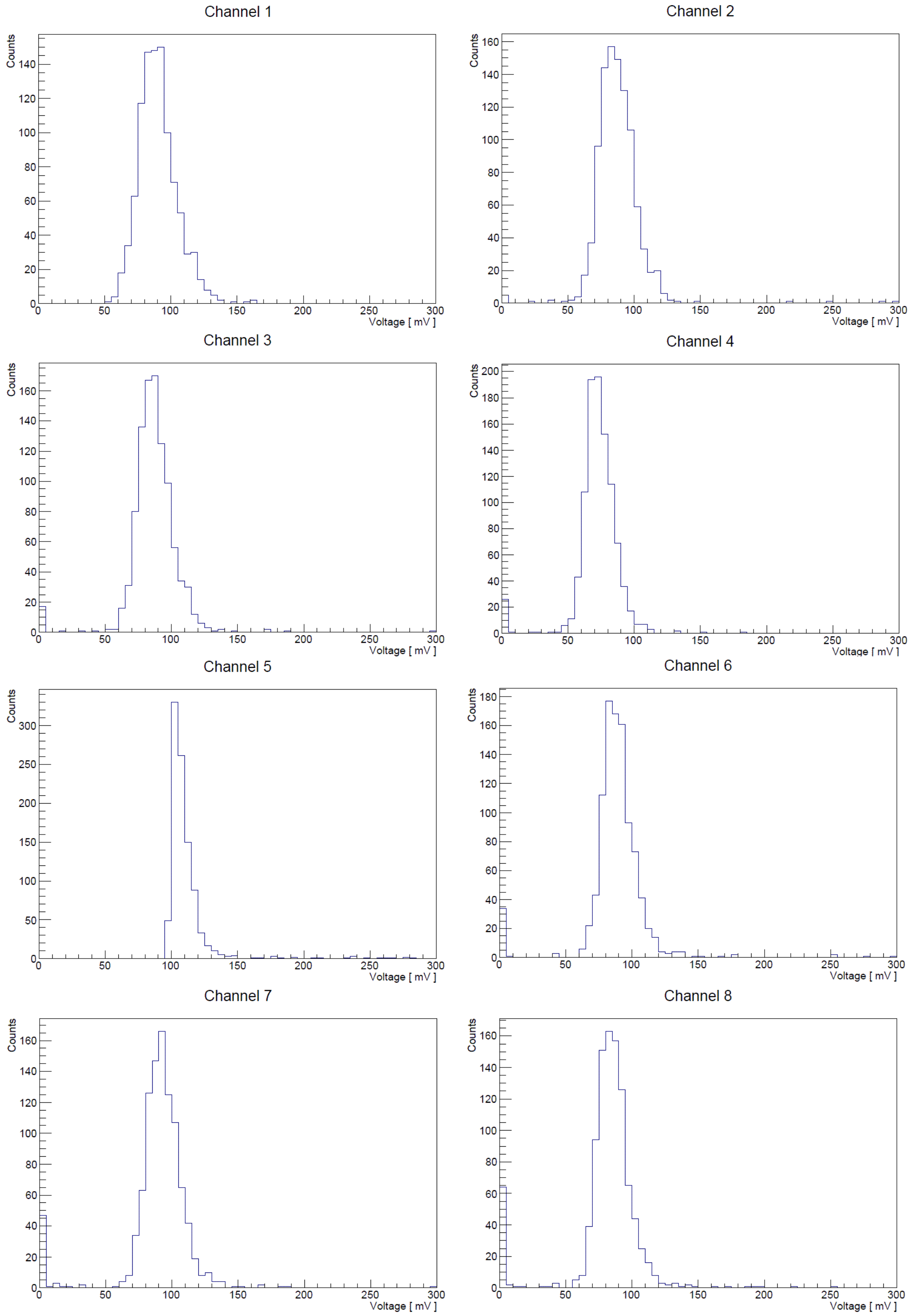

Figure 5.2: Analog SiPM signal amplitude distributions for each channel of Run 8, all collected events included.

Each distribution is very similar to a Gaussian, with the exception of the 5th channel, because of a malfunctioning of the read-out system. Being aware of this, and with the goal of establishing a calibration procedure to be replicated and optimized with future measurements, we chose not to further manipulate it and treat such information with the same procedure applied to the other channels, as described in the follow.

The configuration of Run 8 with a proton beam at 228 MeV is simulated with TRIM (*TRansport of Ions in Matter*), the core of a software bundle called SRIM (*Stopping and Range of Ions in Matter*), which calculates interaction of ions with matter.

The simulation shows that the energy deposition in the initial 4cm of the Bragg Curve is almost constant, within a 5%. So the energy deposition profile obtained from this configuration is interpolated with a linear fit, as shown in Figure 5.3, and the multiplicative factors to rescale each channel are derived. The profile consists in the average of signal pulse amplitudes measured in each finger as a function of the finger position (*channels*).

The uncertainties associated at every point are calculated as the standard deviations.

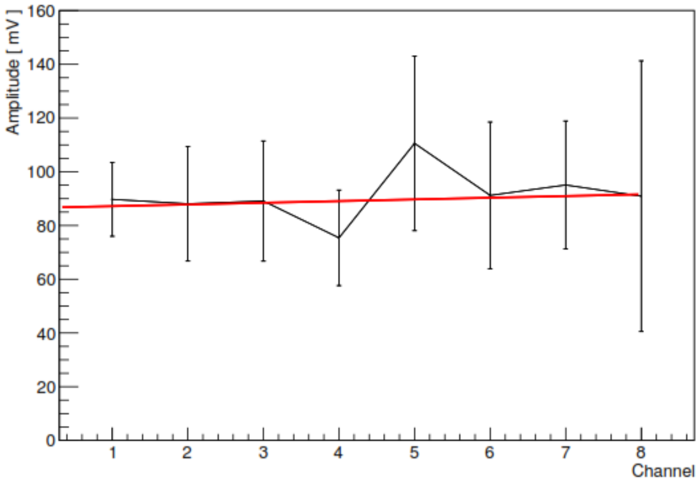

Figure 5.3: Average analog signal amplitudes profile of Run 8 and linear fit. Events with amplitudes lower than 50mV are discarded. The average of the 5th channel is affected by the anomalous behavior of the readout system in this particular run, as discussed in the text.

The values for normalization are obtained with several passages: first the energy deposition profile of the Run 8 is interpolated with a linear fit; the fit is then rescaled to match unity in the first channel. The experimental values from each channel are divided by the corresponding points of the rescaled linear fit. The new channels amplitudes are further normalized using the new value of the first channel as reference. The renormalized values finally span between 0.933 and 1.171 over all 8 channels.

The analysis proceeds with the study of the other configurations in Table 5.1 , from here on data from each channel will be normalized with the respective multiplicative factor. The configuration of Run 4 consists in 8 BC-408 scintillators with a 27.2cm thick absorber positioned between the two scintillators stations, so we expect comparable signals value from the first 4 fingers, and a larger energy deposition inside the last 2 fingers. The 1st, 4th and 7th fingers in AND logic provide the trigger. Figure 5.4 shows the signal amplitude distributions for Run 4.

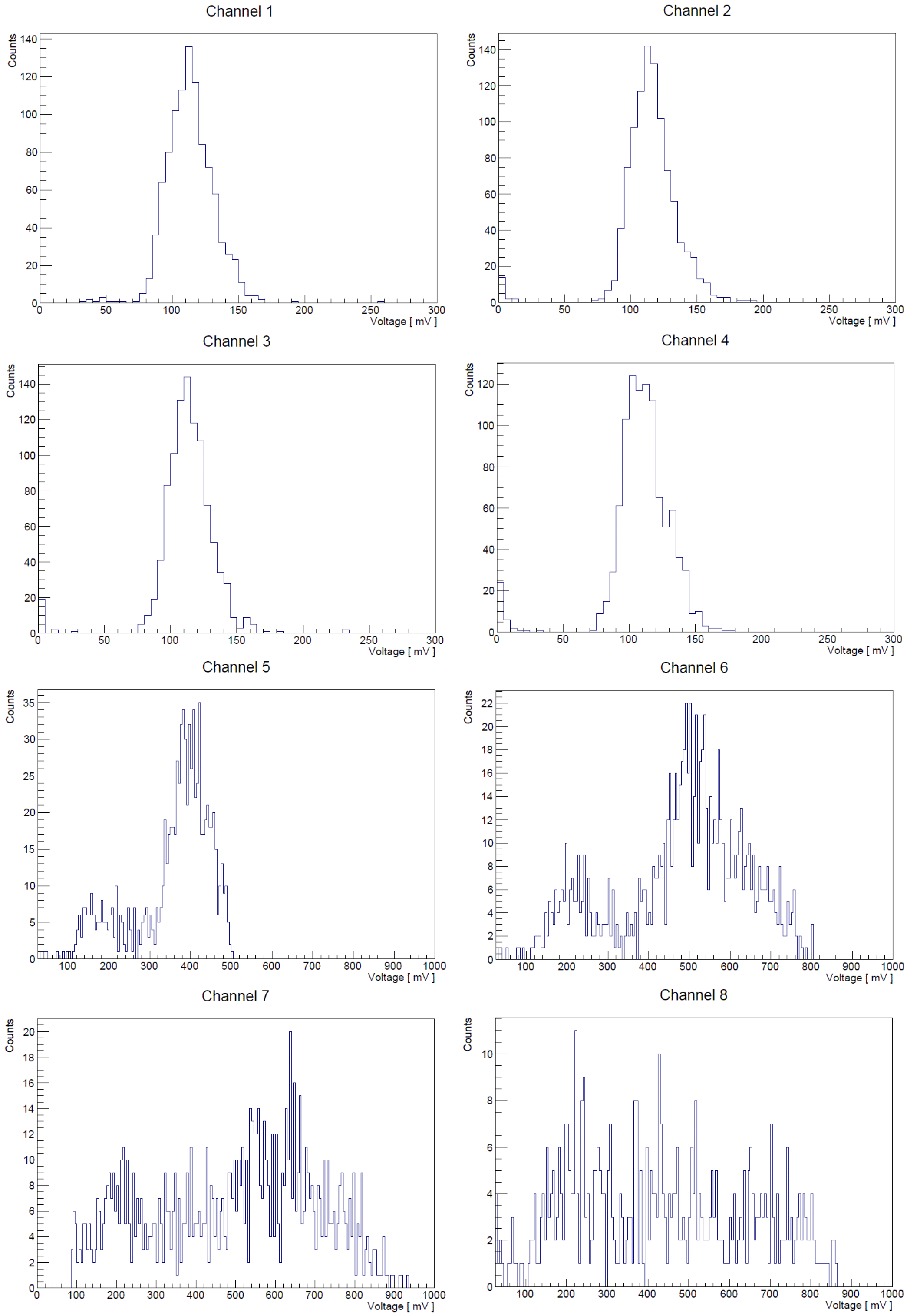

Figure 5.4: Analog SiPM signal amplitude distributions for each channel of Run 4, all collected events included. X axis ranges are adjusted for each channel for sake of clarity.

However, due the complex geometrical configuration of the absorber (made of different blocks of plexiglass with different geometries), and the small active volume of the fingers, it is likely we are actually mixing within the same sample different populations derived by particles following different paths, as Figure 5.4 shows two separated peaks in the last four channels of the maxima distributions.

To better separate protons with different paths, we compare the signals in the two fingers where the proton is expected to come to a complete stop. The scatter plot of Run 4, in Figure 5.5, displays the parameter $y = (V_7 - V_8)/(V_7 + V_8)$ as a function of V_8, where V_i represents signal amplitude for the considered event in the i-th channel, and it is indeed possible to recognize different populations. In the plot, events distributed over the horizontal line at $y \sim 0$ correspond to the events with $V_7 \sim V_8$.

Instead, events distributed over the oblique curve contains events whose energy was released in variable proportions between the two fingers; most likely this area includes protons stopping in 7th or 8th finger.

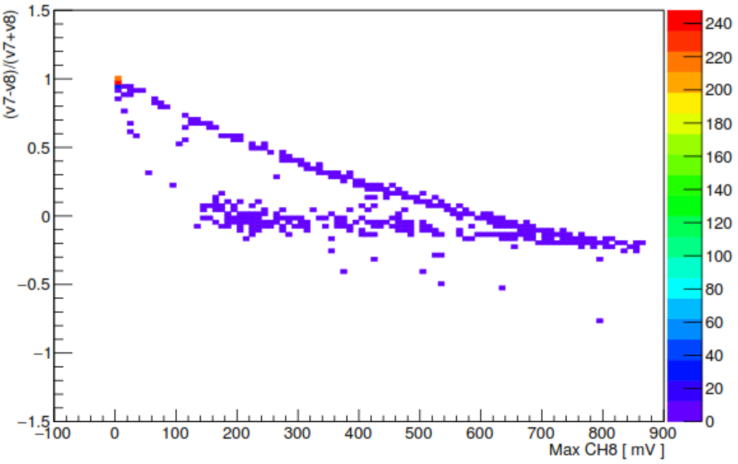

Figure 5.5: Scatter plot of the y parameter as a function of V_8 for Run 4 including all the collected events.

Figure 5.6 shows a comparison between the channels distributions obtained by eliminating events whose maximum is less than 25mV (blue curve with 838 events) and those obtained by selecting events from oblique line of the scatter plot (red curve with 547 events). The first four channels and the 8th channel are modified in the x axis, in order to see the difference between the two distributions. In the 8th channel a lot of events feature a null signal, even if in the figure they are deleted to show the remaining distribution. This feature confirms the idea that the proton beam stops between the 7th and 8th channels.

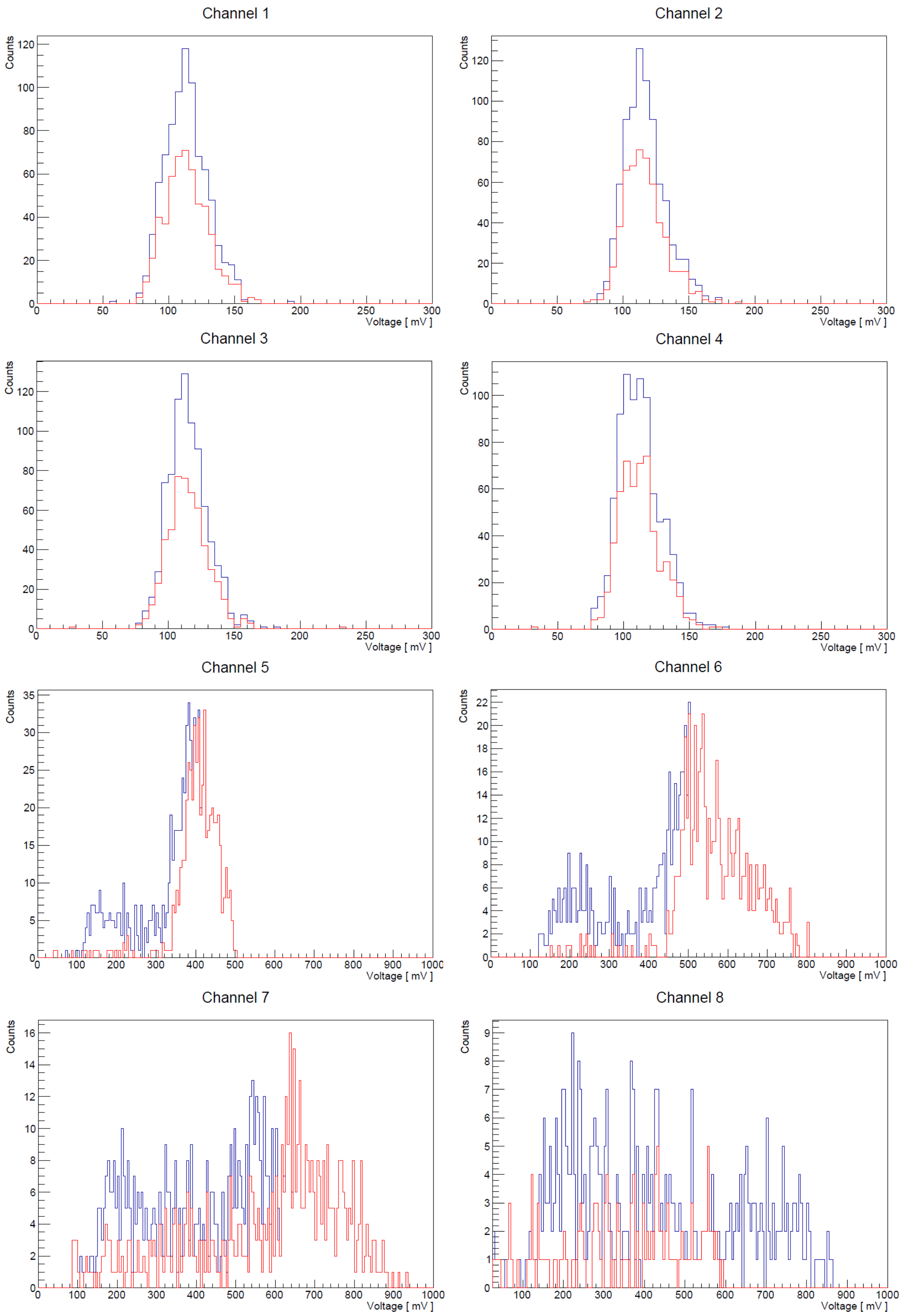

Figure 5.6: Analog SiPM signal amplitude distributions for each channel of Run 4, including events higher than 25mV (blue) and events selected from the scatter plot (red). X axis ranges are adjusted for each channel for sake of clarity.

Finally, it is possible to compare the various curves obtained from the averages of the signals pulse amplitudes with the different cuts (Figure 5.7). The uncertainties linked to averages are calculated as the standard deviation.

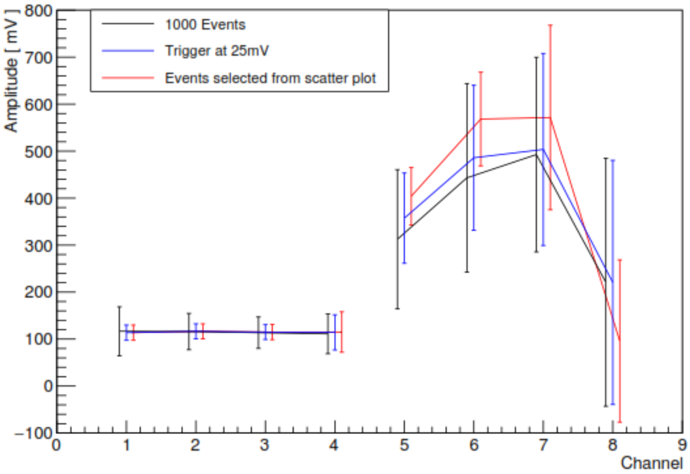

Figure 5.7: Comparison among various signal pulse amplitudes profiles obtained with different methods of Run 4. The curves are slightly shifted for sake of clarity.

In the first four channels, the averages of the signals amplitudes are constant, within errors, and similar for all the methods considered. With the events selected from the scatter plot between the two fingers in which the proton beam stops, the average of the signals amplitudes in 7th channel is the highest while the average of the 8th channel is the lowest, so this method is the best to choose the relevant data.

The follow configurations are studied with the same methods used for Run 4, with relevant differences according to specific features of each Run.

The configuration of Run 5 consists of 8 BC-408 scintillators positioned after a 28.2cm thick absorber with the 1st, 4th and 7th channels triggered. The signal amplitude distributions for each channel are presented in Figure 5.8.

In the channels distributions different peaks are visible, and the reason could be that not all the protons passing through the scintillators had previously crossed the entire absorber. The absorber, in fact, consists of different blocks of Plexiglas of various sizes, so some events collected from the proton beam have crossed all the blocks of the absorber but others have crossed only some parts of it. The peak located at lower amplitudes has an almost constant mean value, around 200mV, in all the channels and represents protons with enough energy to pass through all the scintillators without significantly affecting their energy deposition. Other two peaks appear in the distributions: one appears in the 1st channel and disappears in the 4th showing that a fraction of the protons stops before the 4th finger, the other appears in the 5th channel and disappears in the 7th including protons stopping before the last finger. The latter events considered are most likely those which have passed through the entire absorber thickness.

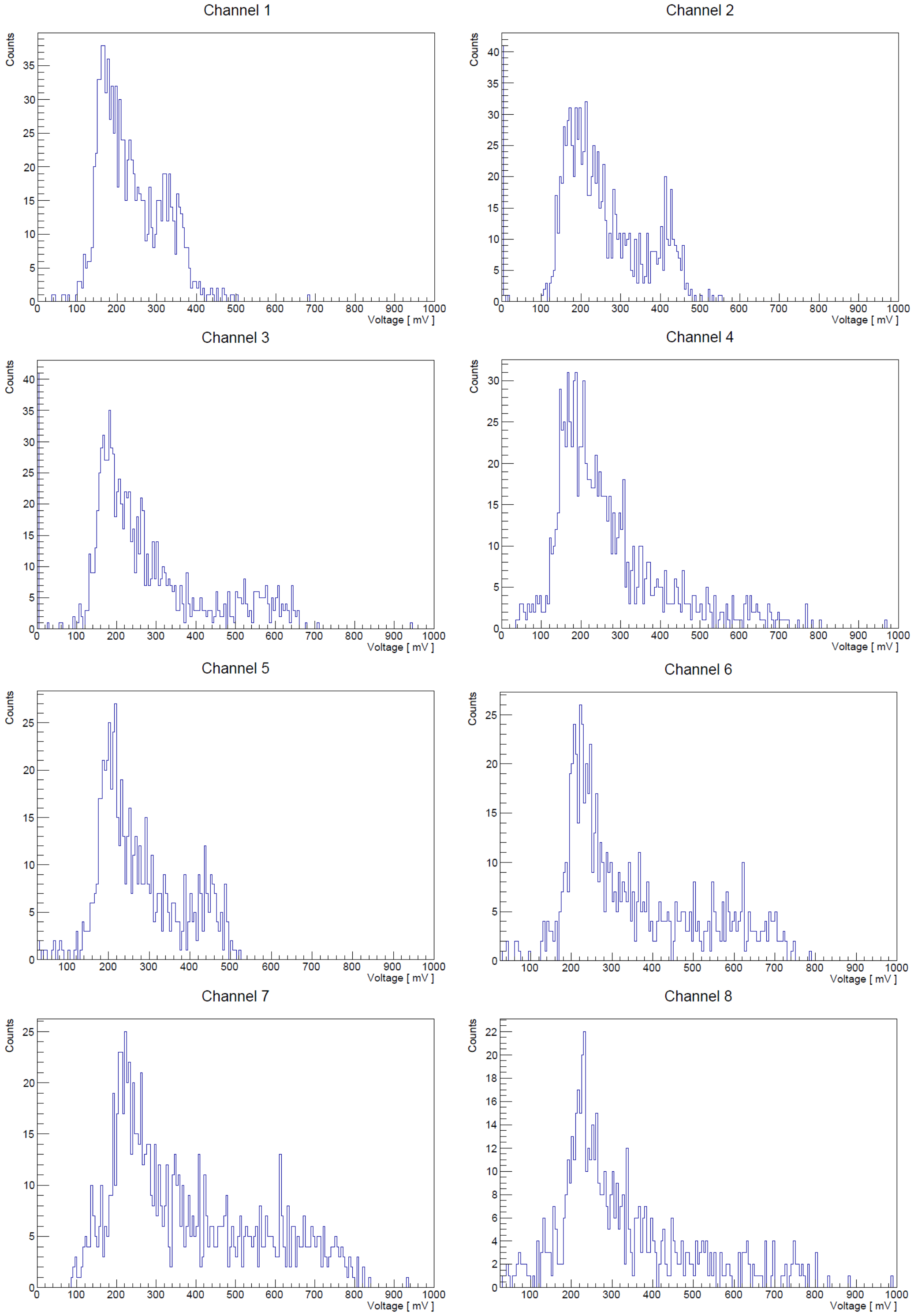

Figure 5.8: Analog SiPM signal amplitude distributions for each channel of Run 5, all collected events included. X axis ranges are adjusted for each channel for sake of clarity.

To verify the hypothesis made earlier, we use two different scatter plots, shown in Figure 5.9: the first displays the parameter $y = (V_6 - V_7)/(V_6 + V_7)$ as a function of V_7, the second displays the parameter $y = (V_3 - V_4)/(V_3 + V_4)$ as a function of V_4. Both the scatter plots highlight two populations, one distributed over the horizontal region $y = 0$ and one slantwise, similarly to those observed for Run 4 (Figure 5.5), plus one described by the relationship $y = -1$, corresponding to $V_6 \sim 0$ in the first case and $V_4 \sim 0$ in the second.

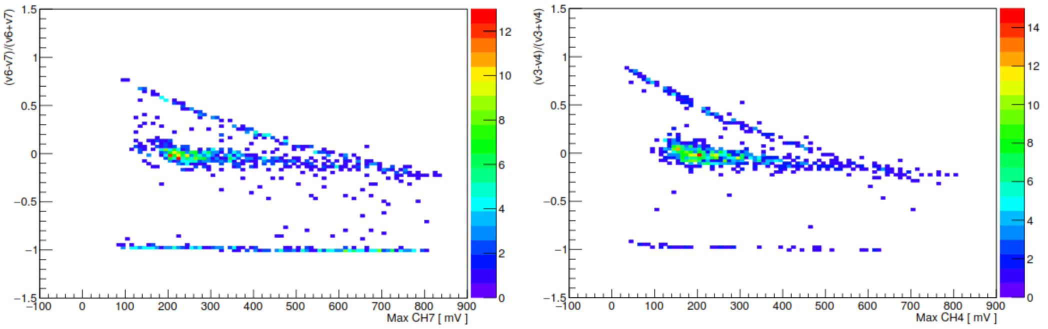

Figure 5.9: Scatter plots of $(V_6 - V_7)/(V_6 + V_7)$ as a function of V_7 (left) and scatter plot of $(V_3 - V_4)/(V_3 + V_4)$ as a function of V_4 (right), for Run 5.

Figure 5.10 presents a comparison between the signal distributions in channels with data obtained by selecting events in various ways.

The blue histogram represents the 674 events that have passed only few centimeters of absorber, in fact the mean of the distributions in all the channels is almost the same, about 200mV. The red histogram represents the 149 events selected from the oblique line of the scatter plot between the 6th and 7th channels where almost the entire energy is released between the 6th and 7th channels, with no signal in 8th channel. The green histogram represents the 124 events selected from the oblique curve of the scatter plot between the 3rd and the 4th channels. Some of the events survive also in the following channels with the same mean of the blue distributions even if they should have stopped. This is probably due to false coincidences, caused by the high proton flux of the beam.

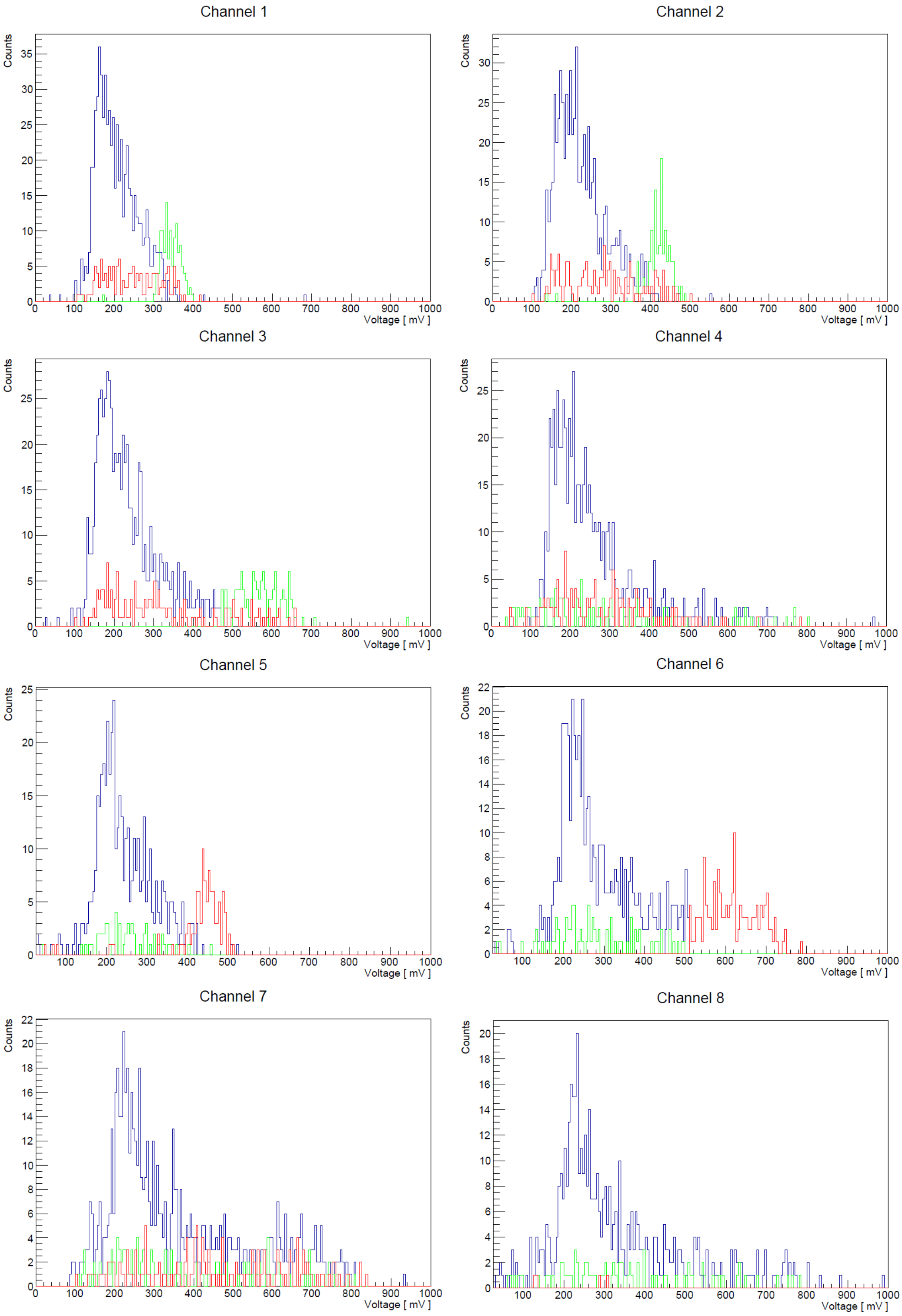

Figure 5.10: Analog SiPM signal amplitude distributions for each channel of Run 5, including events higher than 25mV (blue) and events selected from the 2 scatter plot (red and green). X axis ranges are adjusted for each channel for sake of clarity.

The comparison among the different signal amplitudes profiles are presented in Figure 5.11.

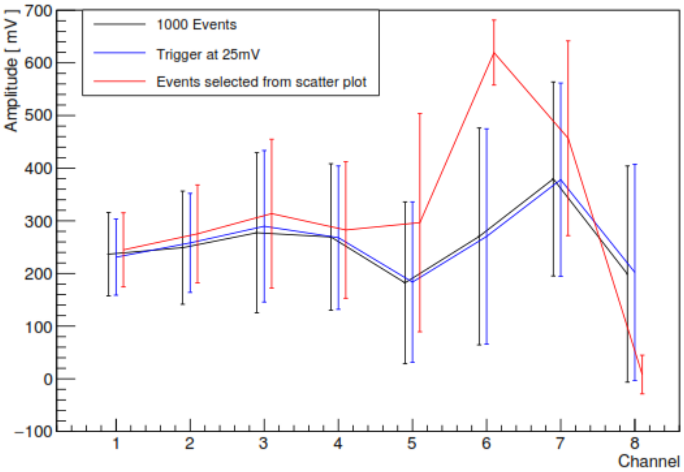

Figure 5.11: Comparison among various signal amplitudes profiles obtained with different methods of Run 5. The curves are slightly shifted for sake of clarity.

From the simulations, the peak of the signal amplitudes profiles is expected between 6th and the 7th channels, so the scatter plot of this configuration displays these two channels and the shape obtained from the events selected from the scatter plot has the best energy deposition profile. The curve with all the events collected has not a profile as clear as the curve obtained from the scatter plot because a significant portion of protons does not releases their entire residual energy inside the fingers and scatter outside: these protons are rejected when we consider the events selected from the oblique curve of the scatter plot.

The configuration of Run 7 is similar to the one of Run 5; the difference is the thickness of the absorber, which is 1cm thicker. Therefore, the entire configuration consists in 29.2cm of absorber plus 8 BC-408 scintillators with 1st and 5th channels triggered at 20mV. Figure 5.12 shows the signal distributions in channels with all the events collected for this configuration. The last two channels are modified in the x axis for the sake of clarity.

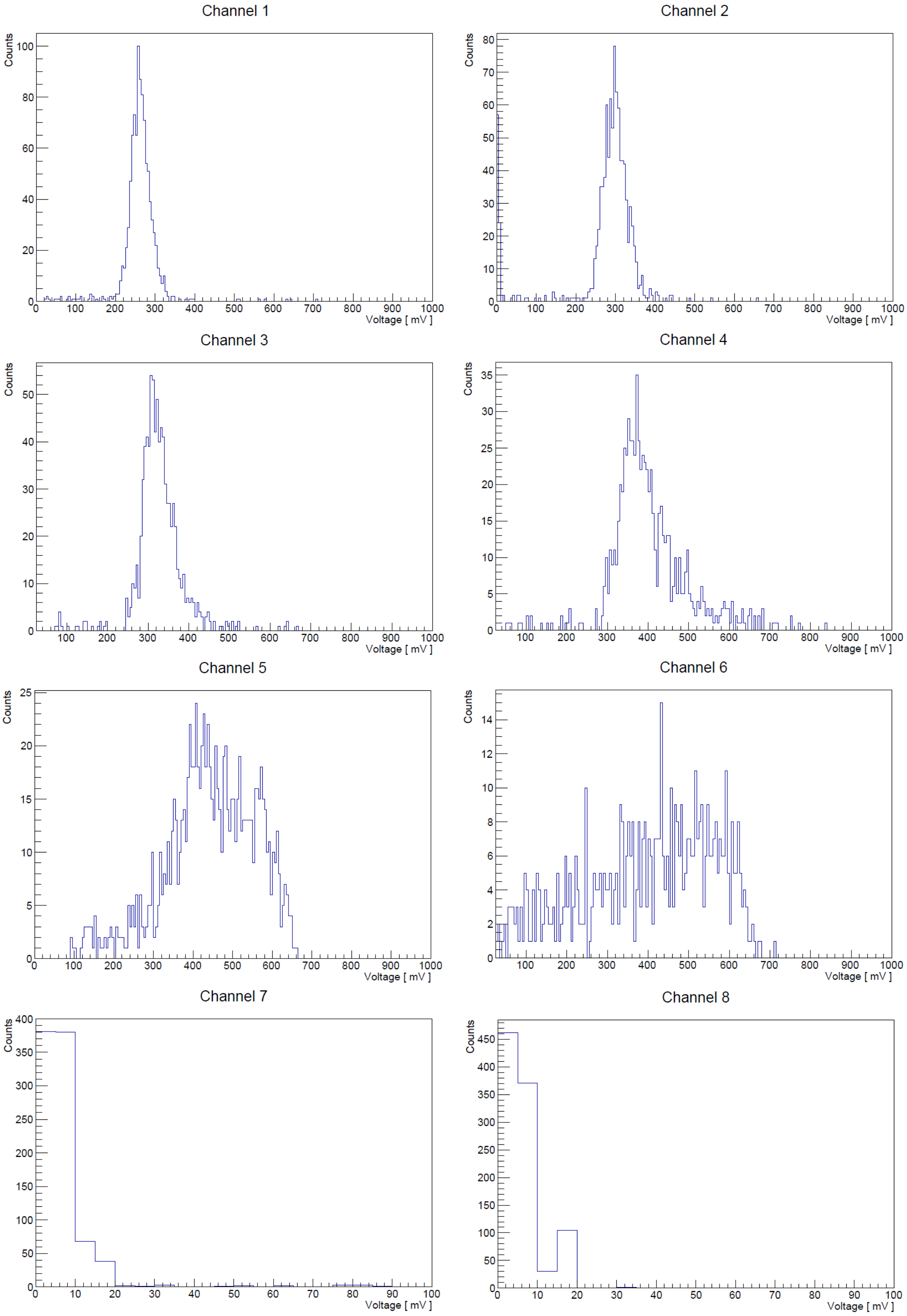

Figure 5.12: Analog SiPM signal amplitude distributions for each channel of Run 7, all collected events included. X axis ranges are adjusted for each channel for sake of clarity.

The shapes of the first four channels distributions are well defined and well interpolated with Gaussian distributions. It is easy to determine the channels in which the proton beam releases the largest part of its energy: in the last two channels, there is no energy release. The scatter plot for this configuration, shown in Figure 5.13, displays the parameter $y = (V_5 - V_6)/(V_5 + V_6)$ as a function of V_6. Only two of the three populations described for Run 5 are distinguishable, as for the configuration of Run 4, and the description is the same of Run 4 with the 5th and 6th channels replacing 7th and 8th channels. The horizontal line at $y = -1$ is not present in this scatter plot because 5th channel is triggered.

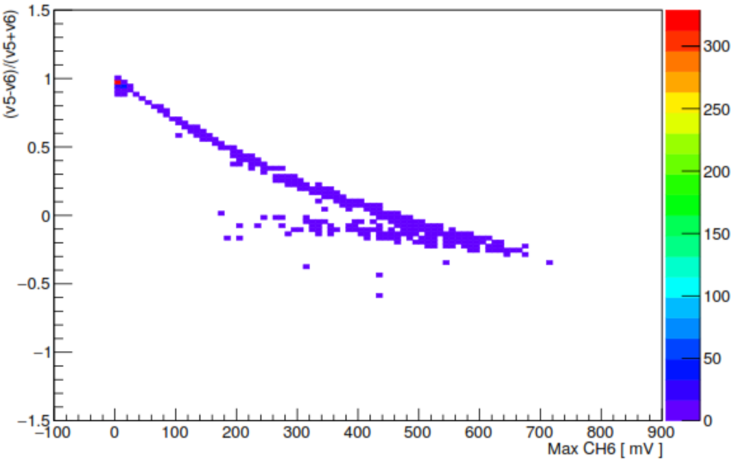

Figure 5.13: Scatter plot of the y parameter as a function of V_6 for Run 7 including all the collected events.

A comparison between the signal distributions in channels obtained by rejecting events whose maximum is lower than 25 mV (blue curve with 759 events) and those obtained by selecting events from oblique curve of the scatter plot (red curve with 490 events), is shown in Figure 5.14.

In the first four channels and the last three the x axis range is modified for clarity. In the 6th channel a large portion of the events collected and selected for the distribution has a signal lower than 25mV, while in the 7th and 8th channels all the events feature a null signal. The fact that the amplitude of a large portion of events is equal to zero in these three channels confirms the results of the simulations and authorizes the discrimination of the events with the cut of the scatter plot.

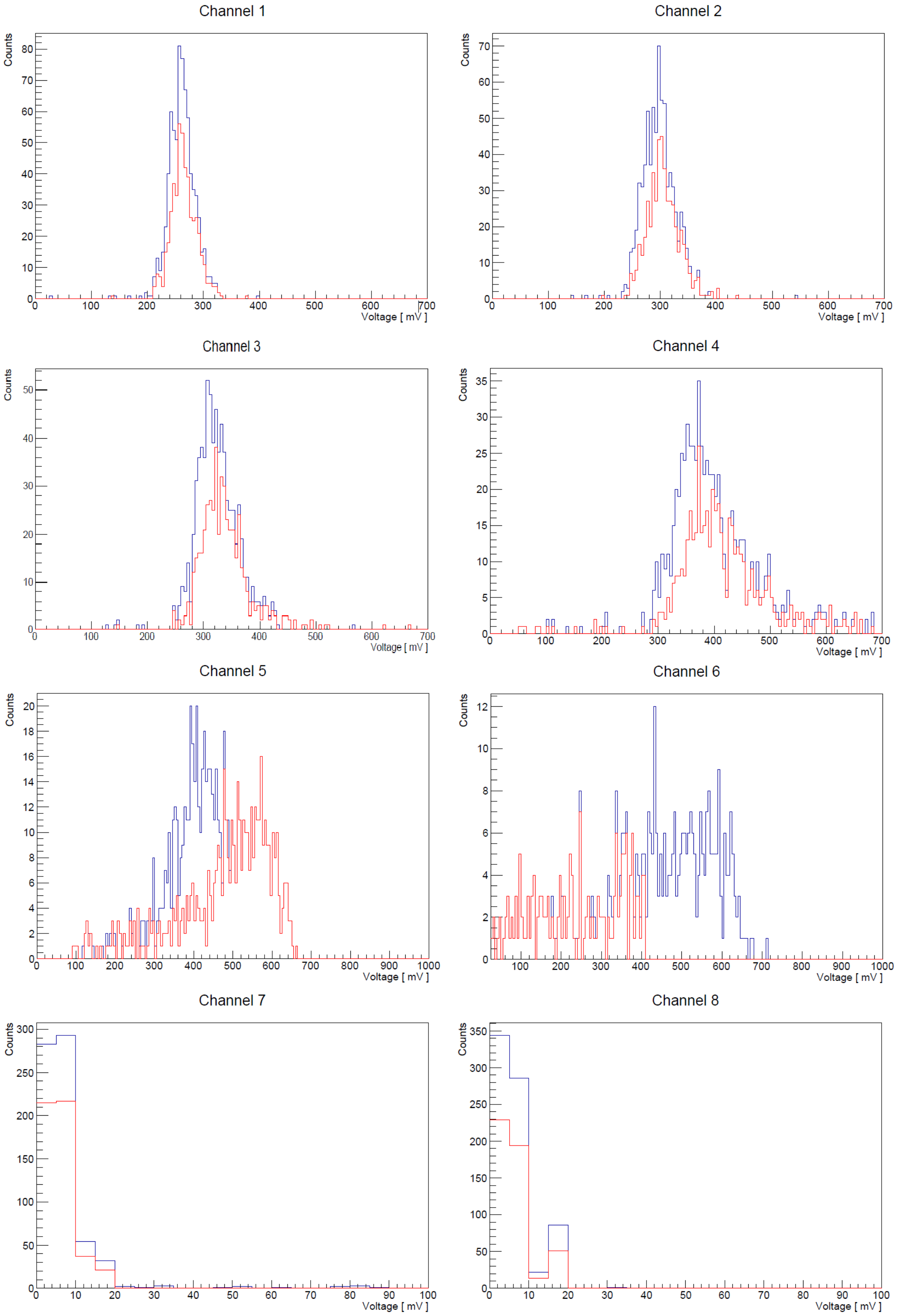

Figure 5.14: Analog SiPM signal amplitude distributions for each channel of Run 7, including events higher than 25mV (blue) and events selected from the scatter plot (red). X axis ranges are adjusted for each channel for clarity.

The comparison among the different signal amplitudes profiles obtained, is shown in Figure 5.15.

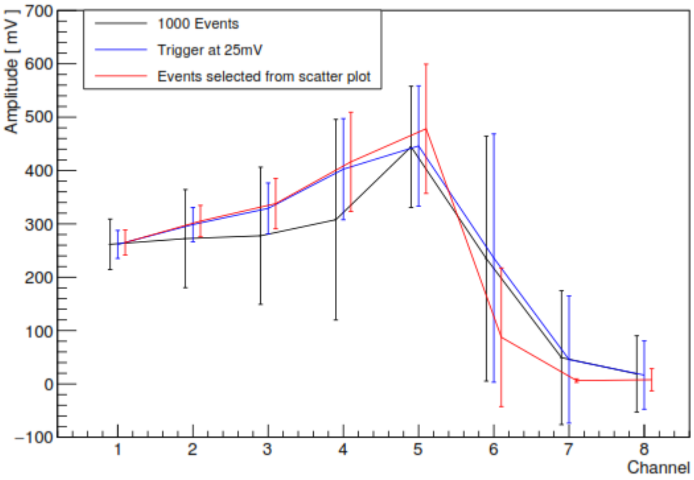

Figure 5.15: Comparison among the signal amplitudes profiles obtained with different selection for Run 7. The curves are slightly shifted for sake of clarity.

In this configuration, the peak of the signal amplitudes profiles is well defined for all the methods considered. The substantial difference consists in the part before the peak: considering the curve displaying all the events collected, the averages of the first 4 channels are similar but this consideration is incorrect because experimentally, immediately before the peak, the curve must increase. So, also in this case the best profile for the configuration is that obtained from the events selected from the oblique curve of the scatter plot, even for the averages of the 7th and 8th channels very close to 0 mV, in fact the proton beam is completely absorbed in the 6th channel.

The configuration of Run 10 consists of 2 BC-420 scintillators not read, 2 BC-420 read and 4 BC-408 scintillators, crossing by a proton beam at 70 MeV. With this beam energy, the peak is ideally between the 3th and the 4th fingers. The energy deposition profile created with all the data collected confirms the hypothesis and Figure 5.16 shows the signal distributions in channels of this configuration. All the considered channels present a distribution similar to a Gaussian distribution even if in the 7th channel there is a second population composed by few events with a higher mean than the principal population.

The scatter plot for this configuration, shown in Figure 5.17, displays the parameter $y = (V_7 - V_8)/(V_7 + V_8)$ as a function of V_8. Three populations are distinguishable being two of them present also in previously discussed cases. The third population includes the events with the signal amplitude of the 8th channel equal to 0 mV.

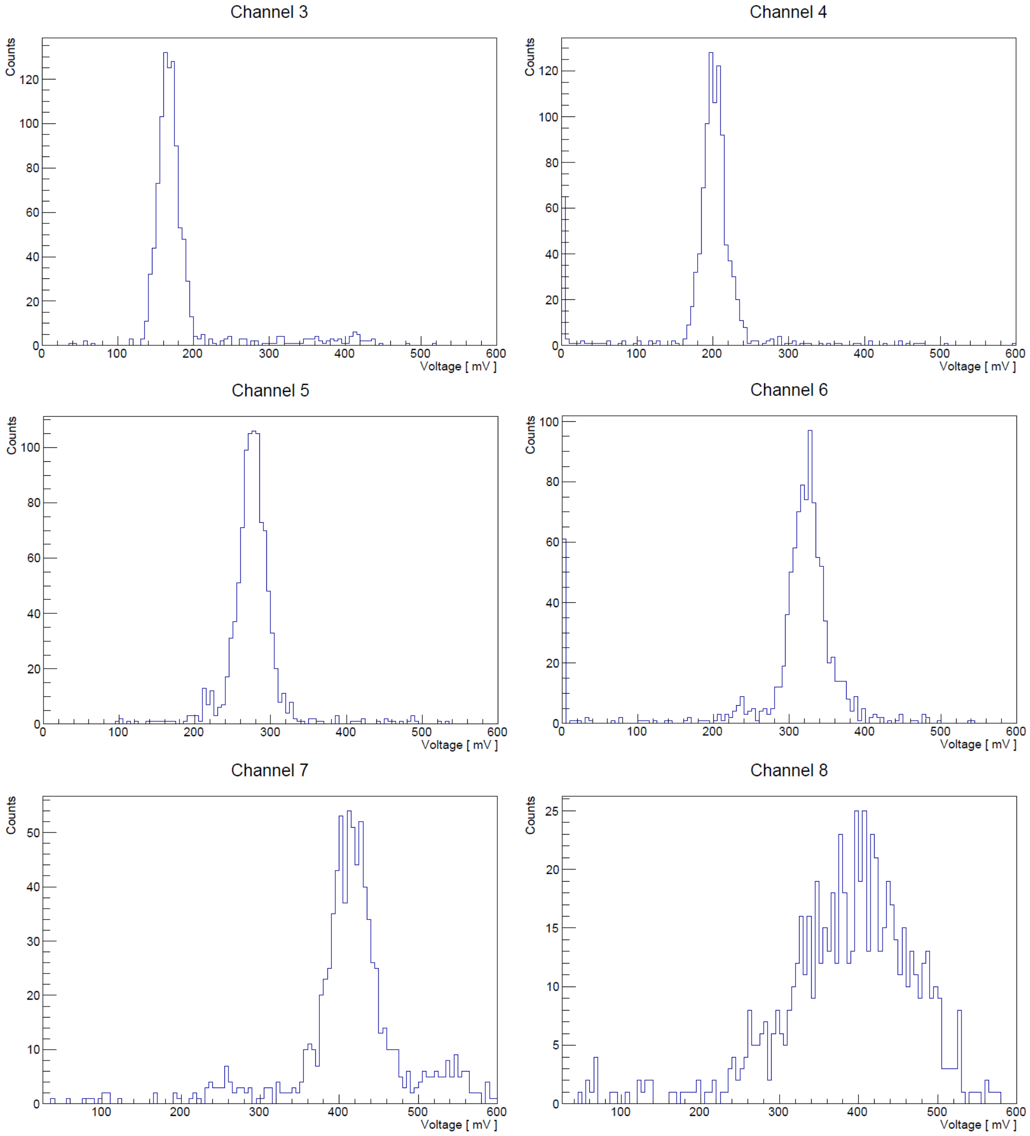

Figure 5.16: Analog SiPM signal amplitude distributions for each channel of Run 10, all collected events included. X axis ranges are adjusted for each channel for sake of clarity.

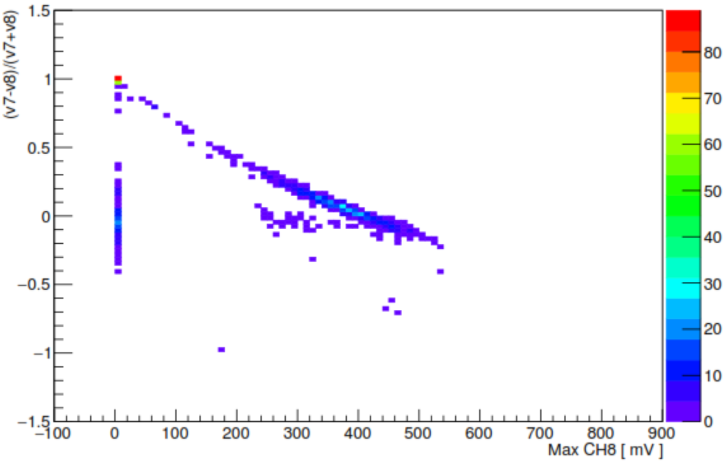

Figure 5.17: Scatter plot of the y parameter as a function of V_8 for Run 10 including all the collected events.

The events selected from oblique curve of the scatter plot and the events whose maximum is lower than 25 mV are almost the same, so Figure 5.18 shows only the signal distributions with the events selected from the scatter plot.

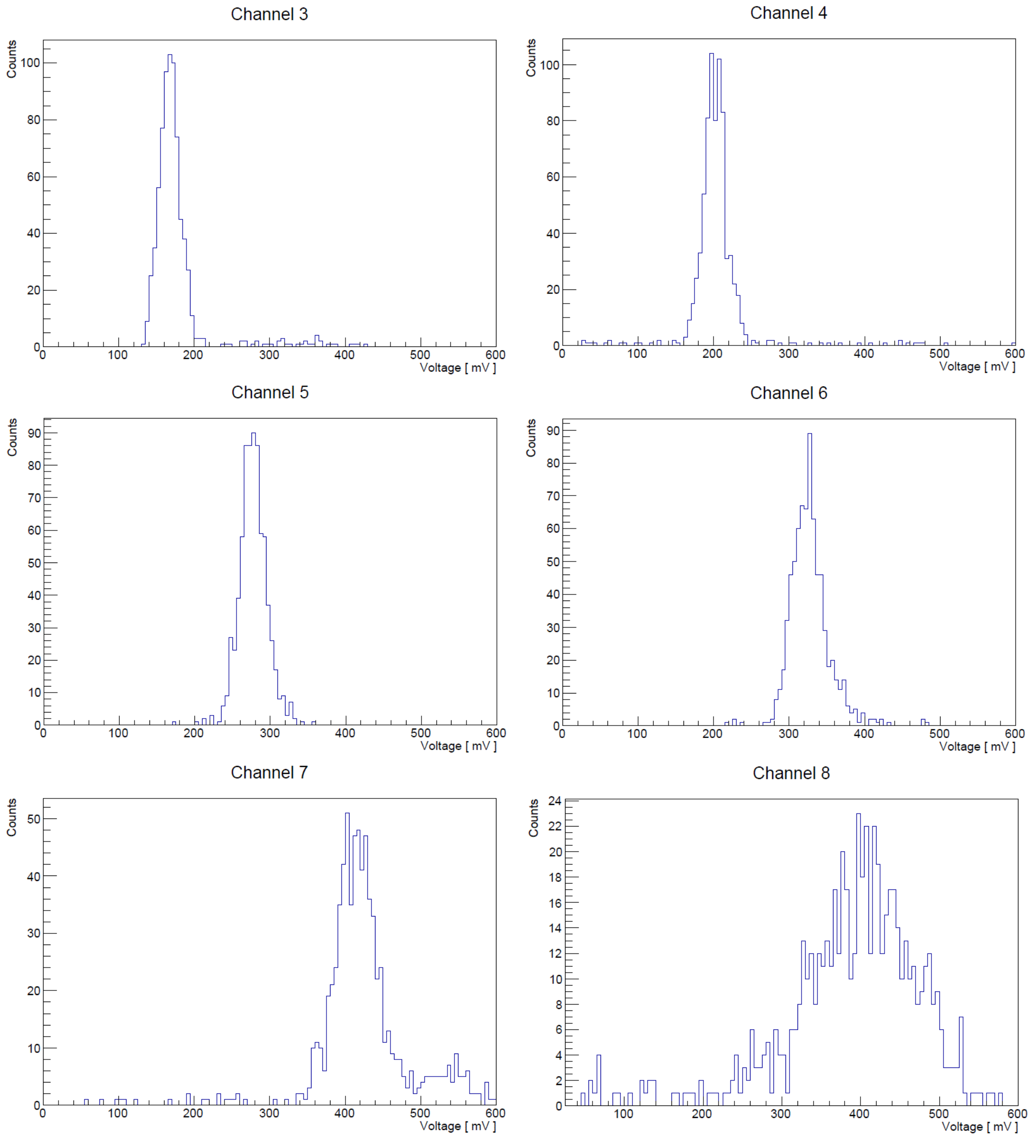
Channel 3

Channel 4

Channel 5

Channel 6

Channel 7

Channel 8

Figure 5.18: Analog SiPM signal amplitude distributions for each channel of Run 10, events selected from the scatter plot are included. X axis ranges are adjusted for each channel for sake of clarity.

Figure 5.19 shows the comparison among the different signal amplitudes profiles obtained. The various profiles considered for the comparison have the same shape. The difference of the curve with the events selected from the oblique curve of the scatter plot consists in a higher peak in the 7th channel associated to a lower average in the 8th channel then in other profiles.

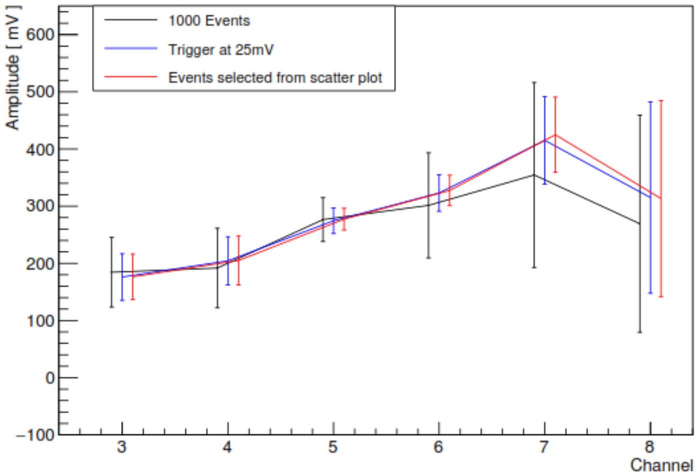

Figure 5.19: Comparison among the signal amplitudes profiles obtained with different methods for Run 10. The curves are slightly shifted for sake of clarity.

The last configuration considered is the one of Run 12 consisting of 8 BC-408 scintillators without absorber, crossed by a proton beam at 35MeV. Such beam is not monochromatic, being obtained by introducing a degrader in front of a 70MeV beam, and we can consider only the first 4 channel for the analysis because the proton beam release all its energy between the 2nd and 3rd fingers. Figure 5.20 shows the signal distributions in channels of this configuration. The channel triggered in this configuration is only the 1st channel.

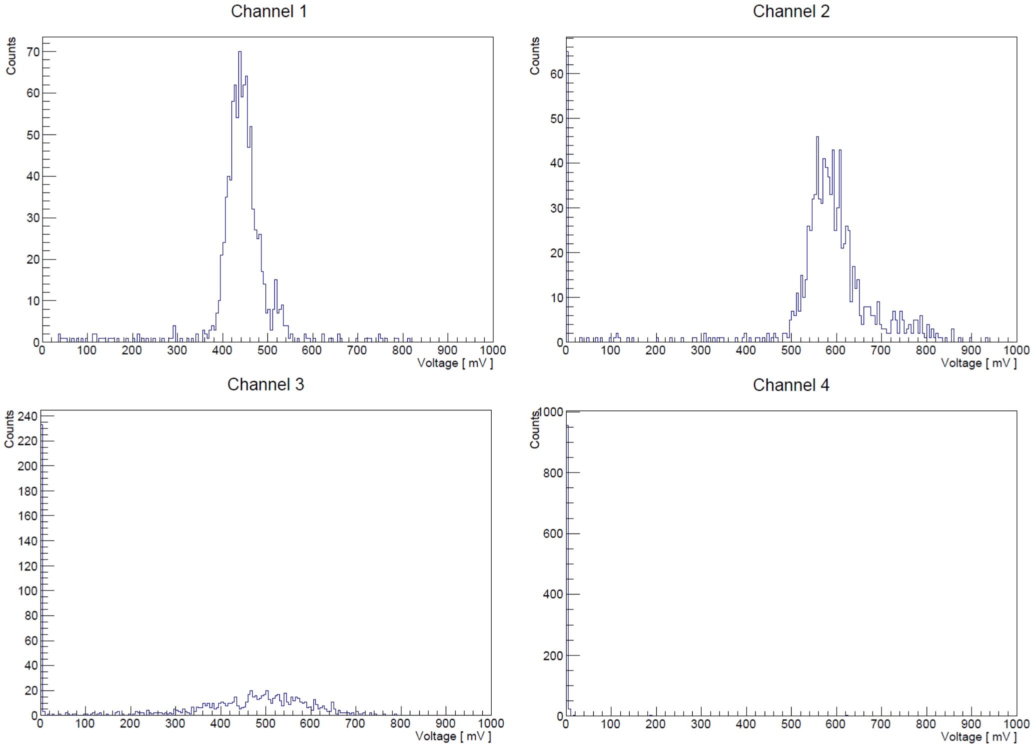

Figure 5.20: Analog SiPM signal amplitude distributions for each channel of Run 12, all collected events included.

The scatter plot for this configuration, shown in Figure 5.21, displays the parameter $y = (V_2 - V_3)/(V_2 + V_3)$ as a function of V_3. Two populations are distinguishable: the population that stands over the oblique curve and the other that stands over the vertical line with the maxima of the signal amplitudes of the 3th channel equal to 0 mV.

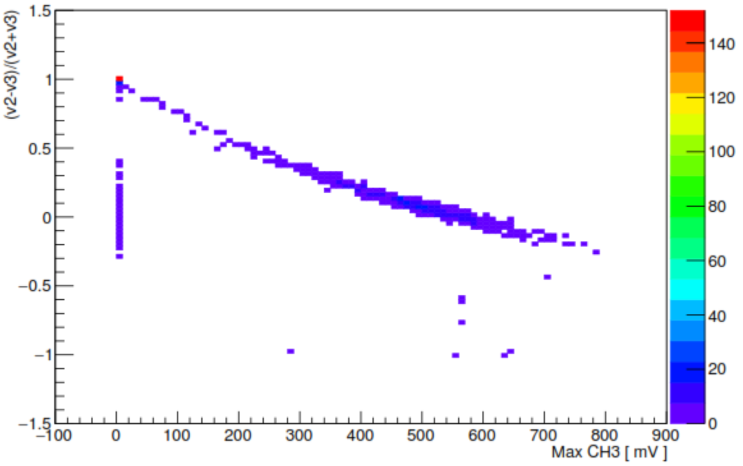

Figure 5.21: Scatter plot of the y parameter as a function of V_3 for Run 12 including all the collected events.

Figure 5.22 shows the signal distribution in channels for this configuration with the events selected from the oblique curve of the scatter plot, previously considered.

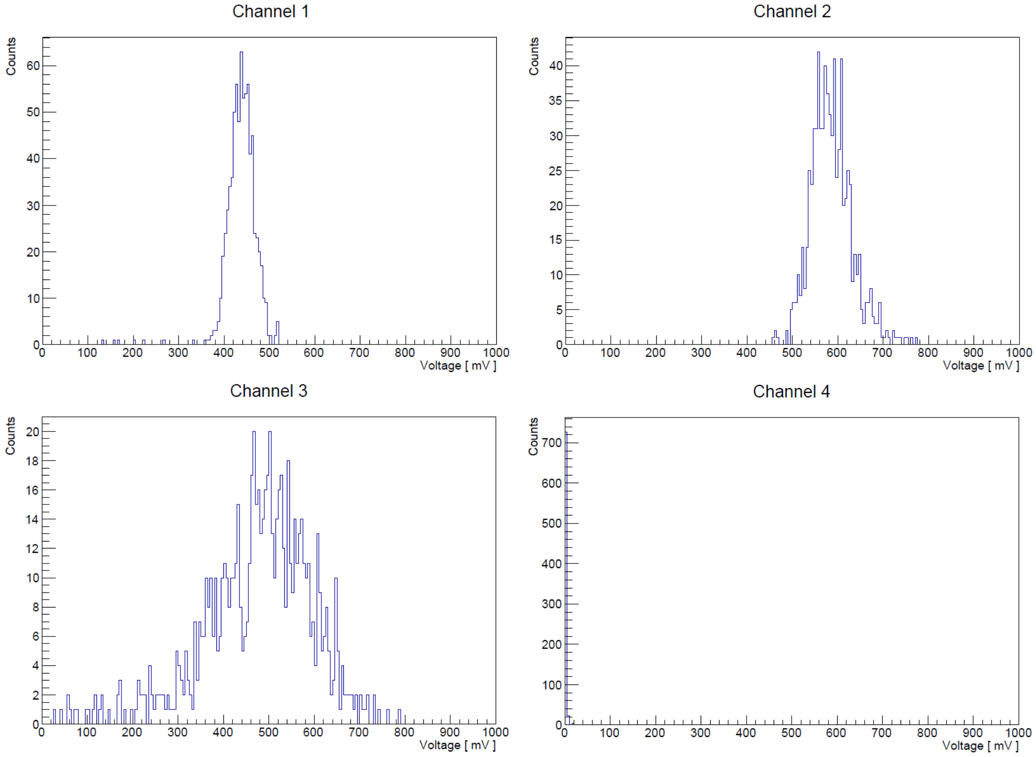

Figure 5.22: Analog SiPM signal amplitude distributions for each channel of Run 12, events selected from the scatter plot are included.

For Run 12, there is not the comparison among the signal distributions in each channel obtained by rejecting events whose maximum is lower than 25mV and those obtained by selecting events from oblique curve of the scatter plot because the number of the events selected are almost the same of the total events.

The comparison among the various curves defined with different methods is shown in Figure 5.23. It confirms the fact that the number of events selected with different methods are almost the same, in fact the curves are superimposed.

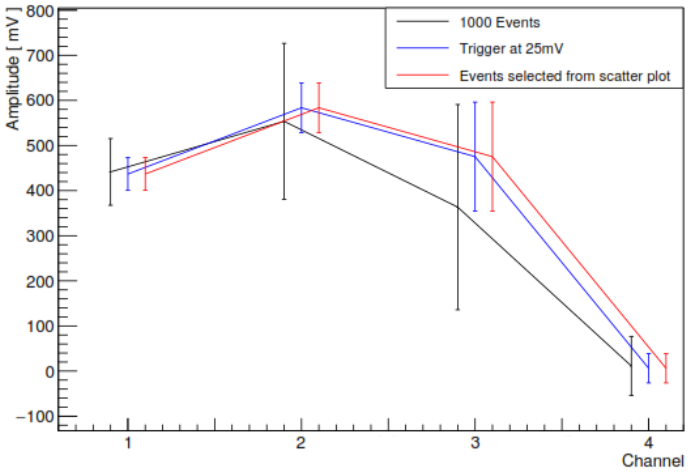

Figure 5.23: Comparison among the signal amplitudes profiles obtained with different methods for Run 12. The curves are slightly shifted for sake of clarity.

5.3 Discussion of the result

A summary of the signal amplitudes measured in the different configurations using a proton beam energy of 228 MeV is shown in Figure 5.24. The averages of the recorded signals amplitudes are plotted as a function of the equivalent length in water crossed by the proton beam, derived from the density of the materials crossed, with the equation:

$$R_{water} = \frac{\rho_{scint} L_{scint} + \rho_{absorber} L_{absorber}}{\rho_{water}} \qquad [\,10\,]$$

where ρ is the density of the material and L its thickness.

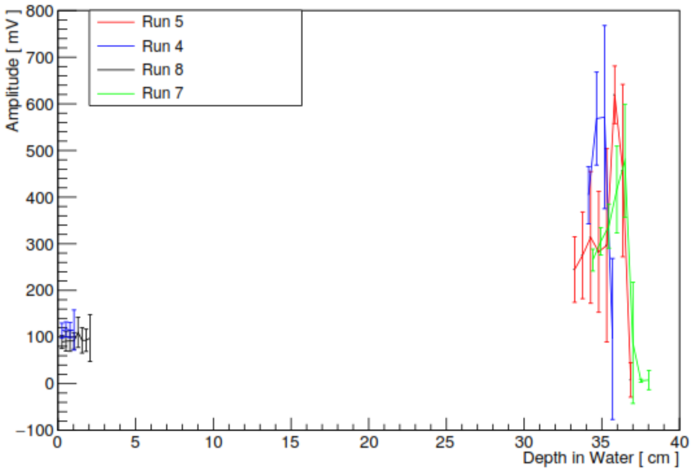

Figure 5.24: Comparison among the signal amplitudes profiles of the configurations with an initial energy of 228 MeV. The events are selected from the various scatter plots for each configuration.

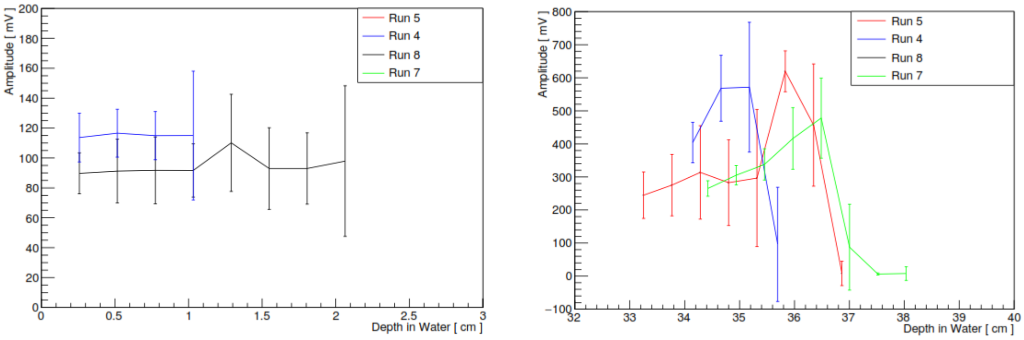

Figure 5.25: Initial and final part of the signal amplitudes profiles shown in the precedent figure.

The left image of Figure 5.25 shows a comparison among the first four channels of similar configurations. The averages of the pulse signal amplitudes of those channels do not coincide precisely, even if the configurations have the same features, but the distance in amplitude between the same channels is approximately constant. The uncertainties associated to the average of the first 3 channels is quite similar, while the 4th channel of Run 4 presents a standard deviation about twice that of Run 8. The ratio between the averages of the two configurations for each channel is about 1.25, so if all the maxima signal amplitudes of the Run 4 were divided for 1.25, the distributions would coincide.

This problem is probably due to the different meteorological conditions from which the SiPM are affected, as the tests were performed on two different days, and a change in the outside temperature can introduce a different characterization of the SiPMs.

6 Conclusions

In medicine, cancer treatment by hadron therapy is not yet a widely used practice, although it is very effective in treating the deep-seated tumors in brain or spinal tissues. The potential of this technique lies in the confinement within a small volume of the hadron energy deposition. The lack of an adequate resolution in the process of acquiring images of the human body before treatment severely limits the potential of such technique. To map the body tissues density with adequate resolution, the Computed Proton Tomography technology uses protons, which feature the same energy deposition profile as the particles used for the therapy, allowing both to maximize the accuracy of the treatment and to reduce the dose deposited in the human body during the imaging process.

The aim of the iMPACT project is to build a pCT scanner composed by a highly segmented energy range calorimeter and a solid state tracking system in order to create a fast and accurate proton Computed Tomography apparatus. All the main components of the design have been evaluated through experiments and simulations, in particular the response gain and linearity of the SiPMs used to read-out the calorimeter scintillators. The single photon signal has a shape well defined with a raise time of about 3 ns, a decay time of about 5 ns. The linearity of the SiPM response is limited by the quenching time; a series of Monte Carlo simulations has been performed in order to quantify this phenomenon.

A first prototype of the range calorimeter was built and extensively tested. The tests show that the apparatus is able to detect and estimate the proton stopping position in a wide energy range, from 35MeV to 230MeV. The SiPM signal distributions of all the test configurations prove the accuracy of the read-out electronic for analog signals, even if it is necessary to improve the calibration among the different modules of the calorimeter to ensure full consistency of collected signals with each other.

An accurate analysis of the configuration of Run 5 clearly shows the ability of the apparatus to distinguish protons that have encountered few millimeters of additional material, even though such excess of material is an unwanted feature of the experimental setup, not foreseen during the planning of the proton beam test, which was focused on the response linearity verification. The capability to identify the presence of additional, unexpected material along the beam path with a post analysis procedure, is a good demonstration of the high sensitivity of the apparatus, even in this early test phase. This preliminary prototype did actually show a proton range resolution which almost matches the final design goal of few mm.

The analysis therefore demonstrates that the hybrid energy-range calorimeter being designed for the iMPACT project has the necessary features to be an effective component to realize a fast and accurate proton Tomography scanner.

7 References

1. **Jemal, A., et al.** *Global cancer statistics, CA: a cancer journal for clinicians.* 2010.

2. **Schardt, D., Elsasser, T. and Schulz-Ertner, D.** *Heavy-ion tumor therapy: physical and radiobiological benefits, Reviews of Modern Physics.* 2010.

3. **Bethe, H.** Zur Theorie des durchgangs schneller korpuskularstrahlen durch materie. *Annalen der Physik.* 1930.

4. **Bloch, F.** Zur bremsung rasch bewegter teilchen beim durchgang durch materie. *Annalen der Physik.* 1933.

5. **Giaccia, A. J. and Hall, E. J.** *Radiobiology for the Radiologist.* s.l. : Lippincott Williams & Wilkins, 2006.

6. **Rutherford, E.** The scattering of α and β particles by matter and the structure of the atom. *The London, Edinburgh, and Dublin Philosophical Magazine and Journal of Science.* 1911.

7. **Zhang, R. and Newhauser, W. D.** The physics of proton therapy. *Physics in medicine and biology.* 2015.

8. **Kleeman, R. and Bragg, W. H.** On the α particles of radium, and their loss of range in passing through various atoms and molecules. *The London, Edinburgh, and Dublin Philosophical Magazine and Journal of Science.* 1905.

9. **Ashkin, J. and Bethe, H.** Passage of Radiations through Matter, Experimental Nuclear Physics, Vol. 1.

10. **Matsinos, E. and Ulmer, W.** Theoretical methods for the calculation of Bragg curves and 3D distributions of proton beams. *The European Physical Journal-Special Topics.* 2010.

11. **Vavilov, P.** Ionization losses of high-energy heavy particles. *Soviet Phys. JETP.* 1957.

12. **Landau, L. D.** On the energy loss of fast particles by ionization. *J. Phys.* 1944.

13. **Janni, J. F.** Proton Range-Energy Tables, 1 keV-10 GeV, Energy Loss, Range, Path Length, Time-of-Flight, Straggling, Multiple Scattering, and Nuclear Interaction Probability. Part I. For 63 Compounds. *Atomic data and nuclear data tables .* 1982.

14. **Sadrozinski, H. F. W. and al.** Toward proton computed tomography. *IEEE Trans. Nucl. Sci.* 2004.

15. **Schneider, U. and al.** First proton radiography of an animal patient. *Med. Phys.* 2004.

16. **Hayat, M.** *Cancer imaging: instrumentation and applications.* s.l. : Academic Press, 2007.

17. **Jermann, M. and Goitein, M.** The relative costs of proton and x-ray radiation therapy. *Clinical onclogy.* 2003.

18. **European Research Council, ERC Consolidator Grants 2014 results.** https://erc.europa.eu/sites/default/files/document/file/erc_2014_cog_full_results_by_domain.pdf. [Online]

19. **Baruffaldi, F.** Studies for a proton tomography scanner. 2017.

20. **Jan, S., et al.** *GATE: a simulation toolkit for PET and SPECT, Physics in medicine and biology.* 2004.

21. **Agostinelli, S., et al.** *Geant4 - a simulation toolkit, Nuclear instruments and methods in physics research section A: Accelerators, Spectrometers, Detectors and Associated Equipment.* 2003.

22. **DRS4 Evaluation Board, PSI.** https://www.psi.ch/drs/DocumentationEN/manual_rev51.pdf. [Online]

23. **Cussol, D.** Hadron therapy, in Ecole Joliot-Curie (30 years) "Physics at the femtometer scale". 2011, p. 46.

24. **Yoon, Myonggeun.** Development and current status of proton therapy for lung cancer in Korea. *Thoracic Cancer. 3.* 2012.